Eigenstrain based Reduced Order Homogenization for Polycrystalline Materials

Xiang Zhang and Caglar Oskay*

Department of Civil and Environmental Engineering
Vanderbilt University
Nashville, TN 37235

Abstract

In this manuscript, an eigenstrain based reduced order homogenization method is developed for polycrystalline materials. A two-scale asymptotic analysis is used to decompose the original equations of polycrystal plasticity into micro- and macroscale problems. Eigenstrain based representation of the inelastic response field is employed to approximate the microscale boundary value problem using an approximation basis of much smaller order. The reduced order model takes into account the grain-to-grain interactions through influence functions that are numerically computed over the polycrystalline microstructure. The proposed approach is also endowed with a hierarchical model improvement capability that allows accurate representation of stress and deformation state within subgrains. The proposed approach was implemented and its performance was assessed against crystal plasticity finite element simulations. Numerical studies point to the capability to efficiently compute the mechanical response of the polycrystal RVEs with good accuracy and the ability to capture stress risers near grain boundaries.

Keywords: Reduced order modeling; computational homogenization; polycrystalline plasticity

1 Introduction

Microstructural morphology significantly affects the mechanical performance of structures made of polycrystalline metals and alloys. While modeling the bulk properties of many metals and alloys have been well established, the connection of the mechanical behavior to the material microstructure is being realized relatively recently. This connection is clearly beneficial for physics-based characterization, and ultimately, control of bulk material properties

*Corresponding author address: VU Station B#351831, 2301 Vanderbilt Place, Nashville, TN 37235. Email: caglar.oskay@vanderbilt.edu

through microstructure design. One significant challenge is the computational complexity of the numerical modeling of polycrystalline microstructures, which exhibit tremendously rich physical phenomena such as grain boundary slip [60], phase transformation [61], morphological complexity (e.g., [54, 18]) and many others.

Evolved from Rice's seminal work on formulations of metal viscoplasticity [56], the crystal plasticity theory describes the deformation mechanisms of metals and alloys by incorporating many microstructural mechanisms including thermal effects [41], mechanical twinning [60], shear band formation [3], martensite formation [61], recrystallization [38], grain boundary slip [8], crack initiation [9] and others. The primary mechanism for plastic deformation remains as the dislocation glide along preferential slip planes, where resolved shear stress acts as the driving force for glide. Finite element analysis of a single crystal was first studied by Peirce, Asaro and Needleman [52, 53] and since then Crystal Plasticity Finite Element Method (CPFEM) have been developed into a powerful tool that can model the response of polycrystalline microstructures under various loading conditions [63]. Using CPFEM, a wide range of physical mechanisms including (but not limited to) grain boundary evolution [31], damage nucleation [5] and creep [62] can be investigated. The CPFEM as a general computational framework has the flexibility to leverage available constitutive formulations that idealize unresolved physical mechanisms, and relies on discretization of the polycrystalline microstructure that allows directly accounting for the stress risers induced by mismatch in grain orientations and other morphological effects.

Multiscale computational methods such as computational homogenization [27], variational multiscale enrichment [49, 50, 70], heterogeneous multiscale method [11], multiscale finite element method [21] and others provide the computational framework to upscale the microstructure scale response to the macroscopic scale. Unfortunately, the high computational complexity of a CPFEM simulation performed over a representative volume element (RVE) typically prohibits straightforward application of these methods to homogenize polycrystal response. The alternative is reduced order modeling of the RVE simulations that provide an approximation to the microscale problem with orders of magnitude computational efficiency (Fig. 1). From the perspective of general heterogeneous media, reduced order methods including the spectral method [1], fast Fourier transform method [47, 43], transformation field analysis [10, 44, 45, 17], proper orthogonal decomposition [34, 66, 20], numerical potentials [67] and the eigendeformation-based homogenization [51, 65, 55, 16], among others have recently been proposed and developed.

Early attempts for reduced order modeling of polycrystalline material are based on the assumption that each grain in the microstructure is subjected to equal and uniform strain (i.e., Taylor bound) or stress (i.e., Sachs bound). While these methods provide homogenized properties to a certain accuracy [39], they do not consider the interactions between individual grains and either fail compatibility (Taylor bound) or equilibrium (Sachs bound). To overcome these drawbacks, Van Houtte and coworkers [22, 23] developed the grain cluster method, in which, the macroscopic deformation is imposed on a cluster of grains instead. In this

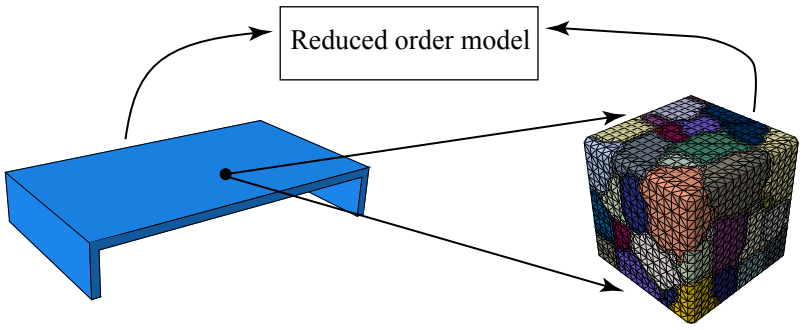

Figure 1: Reduced order model bridges the micro- and macroscale.

context, strain remains homogeneous within each grain but not within the cluster, which relaxes the excessive constraint imposed by the Taylor hypothesis. This approach has been generalized to allow the cluster to have a large number of grains with realistic shapes [64]. While a significant improvement, the grain cluster method still includes limited grain-to-grain interactions. Viscoplastic Self-Consistent (VPSC) method, originally suggested by Kroner [33] and later developed by Lebensohn and Tome [36] has been successfully employed to study polycrystalline plasticity and microstructure evolution. Multiscale simulations that rely on VPSC to describe the behavior at the grain scale have also been performed in the context of implicit finite element analysis [59, 30]. This approach is based on employing the Eshelby solution to approximately account for the microstructural heterogeneity. Eshelby-based core-shell type approximations were used to idealize grain-to-grain interactions [13]. More recently, Lebensohn applied a FFT-based algorithm in conjunction with Green's function method to evaluate the mechanical response of polycrystals [35]. This method solves the equilibrium equation under the constraint of strain compatibility for materials with periodic microstructure and is computationally efficient. However in the FFT-based models that use a uniform grid of Fourier points, the grain boundaries are represented as step-wise discontinuous surfaces [37, 12]. Knezevic and co-workers employed the spectral FFT method, which resulted in two orders of magnitude computational efficiency compared to the conventional crystal plasticity [29, 68, 69]. Further improvements to the computational efficiency has been achieved by use of high performance computing [28].

This manuscript extends the eigendeformation-based reduced-order homogenization method to polycrystal plasticity modeling. The proposed model is based on the eigendeformation-based reduced order homogenization approach previously proposed by Oskay and coworkers [51, 65] to study composite materials. A two-scale asymptotic analysis is used to decompose the original equations of polycrystal plasticity into micro- and macroscale problems. Eigenstrain based representation of the inelastic response field is employed to approximate the microscale boundary value problem using an approximation basis of much smaller order. The proposed approach was implemented and its performance was assessed against crystal plasticity finite element simulations. Numerical studies point to the capability to efficiently compute the mechanical response of the polycrystal RVEs with good accuracy and the ability to capture stress

risers near grain boundaries. The present manuscript presents the following novel contributions: (1) The grain-to-grain interactions are accurately captured through the use of numerical influence functions that directly account for the material microstructure morphology. The use of numerical influence functions (as opposed to those generated through the Eshelby tensor) provides a more accurate distribution of the local stress and strain fields within the microstructure and captures the local variations of the response fields. (2) The modelling approach is enhanced with hierarchical model improvement capability that allows capturing the subgrain stress and deformation states. This information, e.g., elevated stress at grain boundaries may be critical for assessment of fatigue damage initiation. The hierarchical model improvement capability refers to the ability to refine or coarsen the partitioning of the microstructure (i.e., increase or decrease the model order in the ROM) to control the accuracy and efficiency characteristics of the reduced order model. The primary reason for choosing the eigenstrain-based model order reduction approach is that, in a straightforward fashion, it allows capturing the grain-to-grain interactions as well as providing the ability to improve the model prediction through its hierarchical structure as explained below.

The remainder of this manuscript is organized as follows: Section 2 introduces the settings of the two-scale homogenization problem, where the fundamental properties of the response fields and spatial scales are discussed. In Section 3, the governing equations of the system along with a two-scale asymptotic analysis, which lead to a coupled micro- and macroscale problems are presented. In Section 4, the reduced order model for crystal plasticity is formulated. Section 5 details the computational implementation. The numerical verification studies to demonstrate the capability of the present formulation are described in Section 6. Section 7 provides the summary and the future work.

2 Problem statement

Let $\Omega \subset \mathbb{R}^{n_{sd}}$ denote an open bounded domain occupied by a polycrystalline material as schematically illustrated in Fig. 2(a). n_{sd} is the number of space dimensions. The domain is formed by the repetition of a locally periodic, statistically representative volume element (RVE). The material heterogeneity is due to the possible presence of different material phases, constituents, as well as different orientations of grains with otherwise identical molecular composition. The governing equilibrium, stress-strain and kinematic equations that describe the deformation of the polycrystalline domain when subjected to mechanical loading is expressed as ($\mathbf{x} \in \Omega$):

$$\sigma^{\zeta}_{ij,j}(\mathbf{x},t) + b^{\zeta}_{i}(\mathbf{x},t) = 0 \tag{1}$$

$$\sigma^{\zeta}_{ij}(\mathbf{x},t) = L^{\zeta}_{ijkl}(\mathbf{x})(\varepsilon^{\zeta}_{kl}(\mathbf{x},t) - \mu^{\zeta}_{kl}(\mathbf{x},t)) \tag{2}$$

$$\varepsilon^{\zeta}_{ij}(\mathbf{x},t) = u^{\zeta}_{(i,j)}(\mathbf{x},t) \equiv \frac{1}{2}(u^{\zeta}_{i,j} + u^{\zeta}_{j,i}) \tag{3}$$

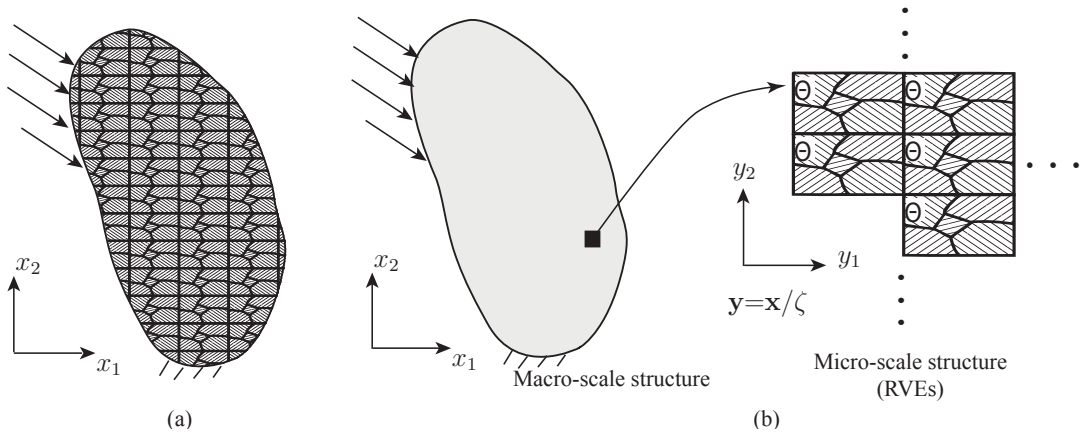

Figure 2: A two-scale problem: macro- and microscale structures.

in which, $\boldsymbol{\sigma}^\zeta$ denotes the Cauchy stress, $\boldsymbol{b}^\zeta$ the body force per unit volume, $\boldsymbol{L}^\zeta$ the tensor of elastic moduli, $\boldsymbol{u}^\zeta$ the displacement and $\boldsymbol{\varepsilon}^\zeta$ the total strain that can be additively decomposed into the elastic and viscoplastic ($\boldsymbol{\mu}^\zeta$) contributions. A comma in the subscript indicates partial spatial derivative and the superscript ζ indicates the oscillatory behavior of the response field due to the microstructural heterogeneity. $\mathbf{x}$ denotes the position vector and t denotes time. The time dependence of the formulation indicates that the viscous behavior of the material is included. While the inertia term is omitted in Eq. (1) for simplicity, the ensuing formulation is also valid for the dynamic response of the polycrystal at the "long" wavelength regime (i.e., when the wavelengths are much longer than the size of the RVE).

It is typical for polycrystalline materials to experience large deformation at the microstructure scale where individual grains significantly deform and rotate, causing texture evolution as a function of applied loads. Large deformation crystal plasticity formulations that capture such texture evolution behavior are readily available (e.g., [53, 39]). The current multiscale formulation is limited to cases in which elastic and inelastic deformations remain small as implicitly implied by Eqs. (2)-(3). By this assumption, the texture remains static during the deformation process and texture evolution is not considered.

Considering the inelastic deformation within a grain is a consequence of dislocation glide induced crystallographic slip along preferred slip orientations, the inelastic strain rate at a material point within a single grain is expressed as:

$$\dot{\mu}_{ij}^\zeta = \sum_{s=1}^{N} \dot{\gamma}^{s,\zeta} Z_{ij}^{s,\zeta} \tag{4}$$

where, $\dot{\gamma}^{s,\zeta}$ is the plastic shearing rate on the s^{th} slip system, N the total number of slip systems, $\mathbf{Z}^{s,\zeta}$ is the Schmid tensor uniquely describing the orientation of the s^{th} slip system as the dyadic product of the slip direction, $\mathbf{n}^{s,\zeta}$, and the normal to the slip plane $\mathbf{m}^{s,\zeta}$, (i.e., $Z_{ij}^{s,\zeta} = n_i^{s,\zeta} m_j^{s,\zeta}$). The resolved shear stress on a slip system, $\tau^{s,\zeta}$, is computed from the stress

tensor using the Schmid tensor as well:

$$\tau^{s,\zeta} = \sigma_{ij}^{\zeta} Z_{ij}^{s,\zeta} \tag{5}$$

The shear strain rate is generally formulated by a flow rule as a function of the resolved shear stress and the slip system strength, $g^{s,\zeta}$ [57]:

$$\dot{\gamma}^{s,\zeta} = \dot{\gamma}^{s,\zeta}(\tau^{s,\zeta}, g^{s,\zeta}) \tag{6}$$

and the evolution of the slip system strength is described by a hardening rule as a function of the shear strain rate and the strength of all the slip systems:

$$\dot{g}^{s,\zeta} = \dot{g}^{s,\zeta}(g^{1,\zeta}, g^{2,\zeta}, ..., g^{N,\zeta}, \dot{\gamma}^{1,\zeta}, \dot{\gamma}^{2,\zeta}, ..., , \dot{\gamma}^{N,\zeta}) \tag{7}$$

which indicates that hardening along a slip system is affected not only by the state on the slip system itself (self-hardening) but all others as well (latent hardening). A number of strength and slip evolution models that specify Eqs. (6) and (7) has been proposed in the literature (see [57] for a comprehensive review). While the reduced order modeling methodology developed in this manuscript does not depend on the particular forms of the evolution equations of the slip or slip system strength, it is beneficial to demonstrate the formulation in the context of a particular form. Using other hardening laws is straightforward and follows the general steps to be described below. Incorporation of some other mechanisms such as twinning [32], which may involve significant texture evolution, violates the small deformation assumption made in the present formulation. Twinning is therefore not considered. In this manuscript, we choose a frequently used flow rule suggested by Rice and Peirce [56, 52, 53] for face-centered cubic (FCC) crystals:

$$\dot{\gamma}^{s,\zeta} = \dot{\gamma}_0 \left(\frac{\left|\tau^{s,\zeta}\right|}{g^{s,\zeta}} \right)^{1/m} \mathrm{sgn}(\tau^{s,\zeta}) \tag{8}$$

where, $\dot{\gamma}_0$ is the reference shear strain rate, m the rate sensitivity parameter. The strength of each slip system is taken to evolve following the hardening rule proposed by Anand [2]:

$$\dot{g}^{s,\zeta} = h_0 \left(\frac{g_{sa}^{s,\zeta} - g^{s,\zeta}}{g_{sa}^{s,\zeta} - g_0^{s,\zeta}} \right) \sum_{s=1}^{N} |\dot{\gamma}^{s,\zeta}| \tag{9}$$

where h_0 is the initial hardening rate, $g_{sa}^{s,\zeta}$ the saturation shear stress, and $g_0^{s,\zeta}$ the initial strength of the s^{th} slip system. The saturation shear stress of the s^{th} slip system is given by:

$$g_{sa}^{s,\zeta} = g_{sa,0}^{s} \left(\sum_{s=1}^{N} |\dot{\gamma}^{s,\zeta}| / \dot{\gamma}_{s0} \right)^{m'} \tag{10}$$

in which, $g_{sa,0}^{s}$, $\dot{\gamma}_{s0}$ and m' are material parameters. All the parameters describing the hard-

ening are orientation independent (i.e., same for all slip systems).

The boundary conditions for the boundary value problem are:

$$u_i^\zeta(\mathbf{x},t) = \bar{u}_i(\mathbf{x},t) \qquad \mathbf{x} \in \Gamma^u \tag{11}$$

$$\sigma_{ij}^\zeta(\mathbf{x},t) n_j = \bar{t}_i(\mathbf{x},t) \qquad \mathbf{x} \in \Gamma^t \tag{12}$$

in which, $\bar{u}_i(\mathbf{x})$ and $\bar{t}_i(\mathbf{x})$ are the prescribed displacement and traction on the boundaries Γ^u and Γ^t, where $\Gamma^u \cup \Gamma^t = \partial\Omega$ and $\Gamma^u \cap \Gamma^t = \emptyset$. $\mathbf{n}$ is the unit normal to Γ^t.

The system of equations given by Eqs. (1)-(12) are analyzed using the asymptotic homogenization method with multiple scales. The idea of the homogenization approach is illustrated in Fig. 2(b), in which the governing equations are decomposed into a homogenized problem defined over the problem domain, Ω, and parameterized by a macroscale coordinate vector, $\mathbf{x}$, and microscale problem defined over the representative volume, Θ, and parameterized by the microscale coordinate vector, $\mathbf{y}$. The scaling relation is $\mathbf{y} = \mathbf{x}/\zeta$ with $0 < \zeta \ll 1$ denoting the size scale parameter given as the ratio between the characteristic length of the RVE and the macrostructure. The microstructure is assumed to be infinitesimal compared to the size of the macroscopic domain. $\mathbf{y}$ therefore is the spatial coordinates of the "blown up" version of the microstructure. The asymptotic analysis is consequently performed at the limit where the scaling parameter vanishes (i.e., scale separable limit) [4, 58]. An arbitrary single-scale response field, $f^\zeta(\mathbf{x})$, is then expressed using the two spatial coordinates as:

$$f^\zeta(\mathbf{x}) = f(\mathbf{x}, \mathbf{y}(\mathbf{x}))) \tag{13}$$

The macroscopic spatial derivative of the response field is given by the chain rule as:

$$f^\zeta_{,x_i}(\mathbf{x}) = f_{,x_i}(\mathbf{x},\mathbf{y}) + \frac{1}{\zeta} f_{,y_i}(\mathbf{x},\mathbf{y}) \tag{14}$$

using the scaling relationship. All response fields are assumed to remain locally periodic throughout the deformation:

$$f(\mathbf{x},\mathbf{y})) = f(\mathbf{x}, \mathbf{y} + \mathbf{k}\hat{\mathbf{y}})) \quad \forall \mathbf{x} \in \Omega \tag{15}$$

where, $\hat{\mathbf{y}}$ is the period of the RVE and $\mathbf{k}$ is a $n_{sd} \times n_{sd}$ diagonal matrix with integer components.

The domain of the RVE denoted as $\Theta \subset \mathbb{R}^{n_{sd}}$ is composed of n_{grain} grains associated with an orientation, lattice type, slip systems and evolution laws governing the slip along the slip systems. Let $\Theta_{gr}^{(i)}$ denote the i^{th} grain within the polycrystal RVE, then $\cup_{i=1}^{n_{grain}} \Theta_{gr}^{(i)} = \Theta$. In this study, full traction continuity is assumed along each grain boundary. We note that accurate modeling of the response mechanisms within grain boundaries may require analysis of them as a separate phase (with thickness on the order of nanometers) or as interface (i.e., cohesive behavior). Such effects are beyond the scope of the current manuscript.

3 Mathematical homogenization with multiple scales

In this section, the multiscale representations of the response functions are used along with the two-scale asymptotic analysis of the original governing equations defined by Eqs. (1)-(12) to formulate the micro- and macroscale problems. An eigenstrain based representation of the inelastic response field is employed to express the microscale problem in an integral form, which forms the basis of the reduced order model described in Section 4. Considering a two-scale asymptotic expansion, the displacement field is expressed as:

$$u_i^{\zeta}(\mathbf{x},t) = u_i^0(\mathbf{x},t) + \sum_{a=1}^{m} \zeta^a u_i^a(\mathbf{x},\mathbf{y},t) + \mathrm{O}(\zeta^{m+1}) \tag{16}$$

in which, the leading order displacement, $\mathbf{u}^0$, is taken to be independent of the microscale coordinates. Substituting Eq. (16) into Eq. (3) yields:

$$\varepsilon_{ij}^{\zeta}(\mathbf{x},t) = \sum_{a=0}^{m} \zeta^a \varepsilon_{ij}^a(\mathbf{x},\mathbf{y},t) + \mathrm{O}(\zeta^{m+1}) \tag{17}$$

where, the first and second order strain components at each order are defined as:

$$\varepsilon_{ij}^a(\mathbf{x},\mathbf{y},t) = u^a_{(i,x_j)}(\mathbf{x},\mathbf{y},t) + u^{a+1}_{(i,y_j)}(\mathbf{x},\mathbf{y},t);\ a = 0,1,... \tag{18}$$

While the first order term of the displacement field in the asymptotic series is independent of the microscale coordinates, the variation of the strain field over the RVE is of order O(1), as indicated by Eq. (17). A comma followed by the micro or macroscale coordinate implies partial derivative with respect to the pertinent coordinate.

Substituting the asymptotic expansion of the strain field (Eq. (17)) into the constitutive relationship yields the stress field in the following asymptotic form:

$$\sigma_{ij}^{\zeta}(\mathbf{x},t) = \sum_{a=0}^{m} \zeta^a \sigma_{ij}^a(\mathbf{x},\mathbf{y},t) + \mathrm{O}(\zeta^{m+1}) \tag{19}$$

in which,

$$\sigma_{ij}^a(\mathbf{x},\mathbf{y},t) = L_{ijkl}(\mathbf{y})\big[\epsilon_{kl}^a(\mathbf{x},\mathbf{y},\mathbf{t}) - \mu_{kl}^a(\mathbf{x},\mathbf{y},\mathbf{t})\big];\ a = 0,1,... \tag{20}$$

The tensor of elastic moduli, L_{ijkl}^{ζ}, is taken to vary locally only (i.e., $L_{ijkl}^{\zeta}(\mathbf{x}) = L_{ijkl}(\mathbf{y})$). This consideration is consistent with the earlier assertion that the body is made of the repetition of an RVE (see Fig. 2(a)). The inelastic strain components are the components of the asymptotic series of the form:

$$\mu_{ij}^{\zeta}(\mathbf{x},t) = \sum_{a=1}^{m} \zeta^a \mu_{ij}^a(\mathbf{x},\mathbf{y},t) + \mathrm{O}(\zeta^{m+1}) \tag{21}$$

To obtain the expressions for the components of the inelastic strain in the asymptotic series,

we proceed by substituting Eq. (19) into resolved shear stress in Eq. (5) and get:

$$\tau^{s,\zeta}(\mathbf{x},t) = \sum_{a=0}^{m} \zeta^a \tau^{s,a}(\mathbf{x},\mathbf{y},t) + \mathrm{O}(\zeta^{m+1}) \tag{22}$$

in which,

$$\tau^{s,a}(\mathbf{x},\mathbf{y},t) = \sigma^a_{ij}(\mathbf{x},\mathbf{y},t) Z^s_{ij}(\mathbf{y}) \tag{23}$$

Similar to the tensor of elastic moduli, the Schmid tensor varies with respect to the local coordinates only, due to the periodicity of the underlying microstructure. The Taylor series expansion of the slip rate in Eq. (8) about $(\tau^{s,0}, g^{s,0})$ gives:

$$\dot{\gamma}^{s,\zeta} = \sum_{p=0}^{\infty}\sum_{q=0}^{\infty} \frac{(\tau^{s,\zeta}-\tau^{s,0})^p (g^{s,\zeta}-g^{s,0})^q}{p!q!} \Big(\frac{\partial^{p+q}\dot{\gamma}^{s,\zeta}}{\partial {\tau^{s,\zeta}}^p \partial {g^{s,\zeta}}^q} \Big)\Big|_{(\tau^{s,0},g^{s,0})} \tag{24}$$

$$= \sum_{a=0}^{m} \zeta^a \dot{\gamma}^{s,a} + \mathrm{O}(\zeta^{m+1}) \tag{25}$$

where, p and q are integers. The first two terms of the slip strength expression are:

$$\dot{\gamma}^{s,0} = \dot{\gamma}_0 \left(\frac{\left|\tau^{s,0}\right|}{g^{s,0}} \right)^{1/m} \mathrm{sgn}(\tau^{s,0}) \tag{26}$$

$$\dot{\gamma}^{s,1} = \frac{\dot{\gamma}_0}{m} \left(\frac{\left|\tau^{s,0}\right|}{g^{s,0}} \right)^{1/m} \left(\frac{\tau^{s,1}}{\tau^{s,0}} - \frac{g^{s,1}}{g^{s,0}} \right) \mathrm{sgn}(\tau^{s,0}) \tag{27}$$

which, combined with Eq. (25), yields the evolution equation of the components of the inelastic strain tensor:

$$\dot{\mu}^a_{ij} = \sum_{s=1}^{N} \dot{\gamma}^{s,a}(\mathbf{x},\mathbf{y},t) Z^s_{ij}(\mathbf{y});\ a = 0,1,... \tag{28}$$

Similarly, expanding Eq. (9) using Taylor series about $(g^{s,0}, \tau^{s,0})$ gives:

$$\dot{g}^{s,\zeta} = \sum_{a=0}^{m} \zeta^a \dot{g}^{s,a} + \mathrm{O}(\zeta^{m+1}) \tag{29}$$

where, the first two terms are given as:

$$\dot{g}^{s,0} = h_0 \left(\frac{g^{s,0}_{sa} - g^{s,0}}{g^{s,0}_{sa} - g^{s,0}_0} \right) \sum_{s=1}^{N} |\dot{\gamma}^{s,0}| \tag{30}$$

$$\dot{g}^{s,1} = \frac{h_0 C}{\tau^{s,0}(g^{s,0}_{sa} - g^{s,0}_0)^2} \left(E\frac{\tau^{s,1}}{\tau^{s,0}} - F\frac{g^{s,1}}{g^{s,0}} \right) \tag{31}$$

in which,

$$g_{sa}^{s,0} = g_{sa,0}^{s} \left(\sum_{s=1}^{N} |\dot{\gamma}^{s,0}| / \dot{\gamma}_{s0} \right)^{m'} \tag{32}$$

and,

$$C := \frac{\dot{\gamma}_0}{m} \left(\frac{|\tau^{s,0}|}{g^{s,0}} \right)^{1/m} \operatorname{sgn}(\tau^{s,0}) \tag{33}$$

$$D := \frac{m'}{\dot{\gamma}_{s0}} g_{sa,0}^{s} \left(\sum_{s=1}^{N} |\dot{\gamma}^{s,\zeta}| / \dot{\gamma}_{s0} \right)^{m'-1} \tag{34}$$

$$E := (1-D)(g_0^{s,0} - g^{s,0}) + (g_{sa}^{s,0} - g^{s,0})(g_{sa}^{s,0} - g_0^{s,0}) \tag{35}$$

$$F := D(g_0^{s,0} - g^{s,0}) + (g_{sa}^{s,0} - g^{s,0})(g_{sa}^{s,0} - g_0^{s,0}) \tag{36}$$

Substituting the asymptotic expansion of the stress field (Eq. (19)) into the equilibrium equation (Eq. (1)), making use of the chain rule (Eq. (14)), and identifying terms with equal order of ζ yields the equilibrium equations at each order of ζ:

$$\mathrm{O}(\zeta^{-1}):\ \sigma_{ij,y_j}^{0}(\mathbf{x},\mathbf{y},t) = 0 \tag{37}$$

$$\mathrm{O}(1):\ \sigma_{ij,x_j}^{0}(\mathbf{x},\mathbf{y},t) + \sigma_{ij,y_j}^{1}(\mathbf{x},\mathbf{y},t) + b_i(\mathbf{x},\mathbf{y},t) = 0 \tag{38}$$

$$\mathrm{O}(\zeta^{a}):\ \sigma_{ij,x_j}^{a}(\mathbf{x},\mathbf{y},t) + \sigma_{ij,y_j}^{a+1}(\mathbf{x},\mathbf{y},t) = 0;\ a = 1,2,... \tag{39}$$

The first order homogenization theory employs the $\mathrm{O}(\zeta^{-1})$ equilibrium equation to formulate the microstructural equilibrium, whereas the homogenized macroscale problem follows from the O(1) equilibrium. It is possible to derive higher order formulations by employing the higher order equilibrium equations (Eq. (39)), which may be important in capturing length scale effects, as well as dispersion phenomena under dynamic loads. While higher order methods hold promise, they typically require higher order continuity and may require special treatment of high order boundary conditions [24, 25, 26]. In this manuscript, the focus is on the formulation of the reduced order crystal plasticity equations in the context of first order homogenization.

Integrating the O(1) equilibrium equation over the RVE domain Θ and exploiting periodicity of stresses over the RVE yields the homogenized equilibrium equation as:

$$\bar{\sigma}_{ij,j}(\mathbf{x},t) + \bar{b}_i(\mathbf{x},t) = 0; \qquad \mathbf{x} \in \Omega \tag{40}$$

in which $\bar{b}_i$ is the RVE average body force; and the overbar indicates the averaging operation over the domain of the RVE. For an arbitrary response function, f:

$$\bar{f}(\mathbf{x},t) \equiv \langle f^{\zeta}(\mathbf{x},t) \rangle_{\Theta} = \frac{1}{|\Theta|} \int_{\Theta} f(\mathbf{x},\mathbf{y},t)\, \mathrm{d}\mathbf{y} \tag{41}$$

where, $|\Theta|$ denotes the volume of the RVE domain Θ.

We further consider boundary conditions that are smooth (i.e., that do not vary at the scale of the microstructure) over the domain of the microstructure. The resulting governing equations for the macroscale problem are summarized in Box 1. The constitutive behavior is expressed as the volume average of the stress field resolved at the RVE scale (i.e., $\bar{\boldsymbol{\sigma}} = \langle \boldsymbol{\sigma} \rangle_\Theta$) and without an explicit constitutive form. The stresses are therefore evaluated at the scale of the RVE, through the microstructure computations as described below. The macroscopic strain provided by the RVE volume averaging is the symmetric gradient of the macroscale displacement (i.e., $\bar{\boldsymbol{\varepsilon}} = \nabla^s \mathbf{u}^0$) due to the periodicity of the displacement field, $\mathbf{u}^1$.

Given: average body force, $\bar{\mathbf{b}}$, boundary conditions, $\bar{\mathbf{u}}, \bar{\mathbf{t}}$ at time $t \in [0, t_0]$

Find: Macroscopic deformation $\mathbf{u}^0 : \bar{\Omega} \times [0, t_0] \to \mathbb{R}^{n_{\text{sd}}}$

- Equilibrium ($\mathbf{x} \in \Omega; t \in [0, t_0]$)

  $\bar{\sigma}_{ij,j}(\mathbf{x}, t) + \bar{b}_i(\mathbf{x}, t) = 0 \qquad \mathbf{x} \in \Omega$

- Constitutive relation ($\mathbf{x} \in \Omega; t \in [0, t_0]$):

  $\bar{\sigma}_{ij}(\mathbf{x}, t) = \langle \sigma^0_{ij}(\mathbf{x}, \mathbf{y}, t) \rangle_\Theta$

- Kinematics ($\mathbf{x} \in \Omega; t \in [0, t_0]$)

  $\bar{\varepsilon}_{ij}(\mathbf{x}, t) = u^0_{(i,x_j)}(\mathbf{x}, t)$

- Boundary conditions:

  $u^0_i(\mathbf{x}, t) = \bar{u}_i(\mathbf{x}, t) \quad \mathbf{x} \in \Gamma^u, t \in [0, t_0] \qquad \bar{\sigma}_{ij}(\mathbf{x}, t) n_j = \bar{t}_i(\mathbf{x}, t) \quad \mathbf{x} \in \Gamma^t, t \in [0, t_0]$

Box 1: Macroscale problem.

Substituting the first order constitutive equation (Eq. (20)) into the $\mathrm{O}(\zeta^{-1})$ equilibrium equation, and using Eq. (18) yields:

$$\{L_{ijkl}(\mathbf{y})[\bar{\varepsilon}_{kl}(\hat{\mathbf{x}}, t) + u^1_{(k,y_l)}(\hat{\mathbf{x}}, \mathbf{y}, t) - \mu^0_{kl}(\hat{\mathbf{x}}, \mathbf{y}, t)]\}_{,y_j} = 0 \tag{42}$$

While Eq. (42) is specialized to an arbitrary but fixed macroscopic position, $\hat{\mathbf{x}}$, is valid for all positions within the macroscopic domain, Ω.

Eq. (42) considered on the domain of an RVE (i.e., $\mathbf{y} \in \Theta$) along with the evolution equations and the periodic boundary condition defined over the RVE boundaries (i.e., $\mathbf{y} \in \partial\Theta$) constitutive a well-defined microscale problem as summarized in Box 2. The microscale problem is evaluated for the microscale displacement field, $\mathbf{u}^1$, considering $\nabla \cdot [\mathbf{L}(\mathbf{y}) : \bar{\boldsymbol{\varepsilon}}(\mathbf{x}, t)]$ as a body force.

Given: material elastic moduli L_{ijkl} and macroscopic strain, $\bar{\epsilon}_{kl}$

Find: Microscopic deformation $\mathbf{u}^1 : \bar{\Theta} \times [0, t_0] \to \mathbb{R}^{n_{\text{sd}}}$ defined at a fixed but arbitrary macroscopic position, $\mathbf{x}$, which satisfy:

- Equilibrium:

$$\{L_{ijkl}(\mathbf{y})[\bar{\varepsilon}_{kl}(\mathbf{x},\mathbf{y},t) + u^1_{(k,y_l)}(\mathbf{x},\mathbf{y},t) - \mu^0_{kl}(\mathbf{x},\mathbf{y},t)]\}_{,y_j} = 0, \quad \mathbf{y} \in \Theta$$

- Kinematics:

$$\dot{\mu}^0_{ij}(\mathbf{x},\mathbf{y},t) = \sum_{s=1}^{N} \dot{\gamma}^{s,0}(\mathbf{x},\mathbf{y},t) Z^s_{ij}(\mathbf{y})$$

- Flow rule:

$$\dot{\gamma}^{s,0}(\mathbf{x},\mathbf{y},t) = \dot{\gamma}_0 \left(\frac{\left|\tau^{s,0}(\mathbf{x},\mathbf{y},t)\right|}{g^{s,0}(\mathbf{x},\mathbf{y},t)} \right)^{1/m} \operatorname{sgn}\left(\tau^{s,0}(\mathbf{x},\mathbf{y},t)\right)$$

- Hardening rule:

$$\dot{g}^{s,0}(\mathbf{x},\mathbf{y},t) = h_0 \left(\frac{g^{s,0}_{sa} - g^{s,0}(\mathbf{x},\mathbf{y},t)}{g^{s,0}_{sa} - g^s_0} \right) \sum_{s=1}^{N} \left|\dot{\gamma}^{s,0}(\mathbf{x},\mathbf{y},t)\right|$$

- Schmid's law:

$$\tau^{s,0}(\mathbf{x},\mathbf{y},t) = \sigma^0_{ij}(\mathbf{x},\mathbf{y},t) Z^s_{ij}(\mathbf{y})$$

- Θ-periodic boundaries on $\mathbf{y} \in \Gamma_\Theta$

Box 2: Microscale problem based on mathematical homogenization.

4 Eigenstrain-based reduced order model

The microscale boundary value problem defined over the RVE summarized in Box 2 along with the macroscale boundary value problem defined over the domain of the problem, Ω, is the first order computational homogenization (also called FE^2, see [15, 14]) applied to polycrystalline plasticity. The micro- and macroscale problems are nonlinear and strongly coupled. When the finite element method (FEM) is employed to numerically evaluate the problem, a separate RVE is associated with each quadrature point of the macroscale discretization. The macroscale constitutive response at a quadrature point is computed as the volume averaging of the microscale stress field obtained through the numerical evaluation of the microscale boundary value problem on the RVE of the quadrature point. In view of the fact that many polycrystalline RVEs require a very large degree of freedom (e.g., $\mathrm{O}(10^5) - \mathrm{O}(10^6)$) to resolve the complicated microstructural topology, direct evaluation of the multiscale system defined in Boxes 1 and 2 is computationally prohibitive. In this study, we employ the eigenstrain idea to develop a reduced order approximation to the microscale boundary value problem, which

starts by decomposing the microscale displacement as ([47, 51]):

$$u_i^1(\mathbf{x},\mathbf{y},t) = H_{ikl}(\mathbf{y})\bar{\varepsilon}_{kl}(\mathbf{x},t) + \int_\Theta h_{ikl}(\mathbf{y},\hat{\mathbf{y}})\mu_{kl}^0(\mathbf{x},\hat{\mathbf{y}},t)d\hat{\mathbf{y}} \tag{43}$$

where $\mathbf{H}(\mathbf{y})$ and $\mathbf{h}(\mathbf{y},\hat{\mathbf{y}})$ are the elastic and eigenstrain influence functions with symmetry on the second and third indices [25] (i.e., $H_{ikl} = H_{ilk}$, $h_{ikl} = h_{ilk}$). The first component of Eq. 43 is due to the classical separation of variables considered in linear elastic computational homogenization [4]. The second component is obtained based on the Green's function approach, in which the inelastic strain field is viewed as the spatially variable "force" acting on the microstructure [7]. The detailed evaluation of the influence functions are further discussed in Section 5.1. Substituting Eq. (43) into Eq. (42) the microscale equilibrium can be written in the form incorporating the influence functions as:

$$\left\{ L_{ijkl}(\mathbf{y})\left[A_{klmn}(\mathbf{y})\bar{\epsilon}_{mn}(\mathbf{x},t) + \int_\Theta a_{klmn}(\mathbf{y},\hat{\mathbf{y}})\mu_{mn}^0(\mathbf{x},\hat{\mathbf{y}},t)\mathrm{d}\hat{\mathbf{y}}\right]\right\}_{,y_j} = 0 \tag{44}$$

where

$$A_{klmn}(\mathbf{y}) = G_{klmn}(\mathbf{y}) + I_{klmn} \tag{45}$$

$$a_{klmn}(\mathbf{y},\hat{\mathbf{y}}) = g_{klmn}(\mathbf{y},\hat{\mathbf{y}}) - I_{klmn}\delta(\mathbf{y}-\hat{\mathbf{y}}) \tag{46}$$

with $G_{klmn}(\mathbf{y}) = H_{(k,y_l)mn}(\mathbf{y})$ and $g_{klmn}(\mathbf{y},\hat{\mathbf{y}}) = h_{(k,y_l)mn}(\mathbf{y},\hat{\mathbf{y}})$ being the elastic and eigenstrain polarization functions, respectively. It is straightforward to see that both $\mathbf{G}(\mathbf{y})$ and $\mathbf{g}(\mathbf{y},\hat{\mathbf{y}})$ possess the minor symmetry (i.e., $G_{ijkl} = G_{ijlk}$, $G_{ijkl} = G_{jikl}$, $g_{ijkl} = g_{ijlk}$, $g_{ijkl} = G_{jikl}$) due to the symmetry on the second and third indices of the influence functions. δ is the Dirac delta function, and $\mathbf{I}$ the fourth order identity tensor. Substituting Eq. (43) into Eq. (18) gives:

$$\varepsilon_{ij}^0(\mathbf{x},\mathbf{y},t) = A_{ijkl}(\mathbf{y})\bar{\varepsilon}_{kl}(\mathbf{x},t) + \int_\Theta g_{ijkl}(\mathbf{y},\hat{\mathbf{y}})\mu_{kl}^0(\mathbf{x},\hat{\mathbf{y}},t)\,\mathrm{d}\hat{\mathbf{y}} \tag{47}$$

RVE averaging of Eq. (47) shows that the influence functions must satisfy the following constraints:

$$\langle G_{ijkl}\rangle_\Theta = 0; \qquad \frac{1}{|\Theta|}\int_\Theta g_{ijkl}(\mathbf{y},\hat{\mathbf{y}})\,\mathrm{d}\hat{\mathbf{y}} = 0 \tag{48}$$

It is trivial to see that Eq. (48) is satisfied for periodic influence functions.

The computational complexity of solving the RVE problem is reduced by introducing the following discretization of the first order inelastic strain (i.e., eigenstrain) and stress fields:

$$\mu_{ij}^0(\mathbf{x},\mathbf{y},t) = \sum_{\alpha=1}^{n} N^{(\alpha)}(\mathbf{y})\mu_{ij}^{(\alpha)}(\mathbf{x},t) \tag{49}$$

$$\sigma_{ij}^{0}(\mathbf{x},\mathbf{y},t)=\sum_{\alpha=1}^{n}N^{(\alpha)}(\mathbf{y})\sigma_{ij}^{(\alpha)}(\mathbf{x},t) \tag{50}$$

where $n \geq n_{grain}$ is an integer that indicates the order of the reduced order model, n_{grain} the number of grains within the RVE, $N^{(\alpha)}$ the shape functions, $\boldsymbol{\mu}^{(\alpha)}$ and $\boldsymbol{\sigma}^{(\alpha)}$ the nonlocal eigenstrain and stress coefficients, respectively. The nonlocal coefficients are expressed in terms of nonlocal weighting functions:

$$\mu_{ij}^{(\alpha)}(\mathbf{x},t)=\int_{\Theta}\psi^{(\alpha)}(\mathbf{y})\mu_{ij}^{0}(\mathbf{x},\mathbf{y},t)\,\mathrm{d}\mathbf{y} \tag{51}$$

$$\sigma_{ij}^{(\alpha)}(\mathbf{x},t)=\int_{\Theta}\psi^{(\alpha)}(\mathbf{y})\sigma_{ij}^{0}(\mathbf{x},\mathbf{y},t)\,\mathrm{d}\mathbf{y} \tag{52}$$

The shape functions, $N^{(\alpha)}$, differ from the standard finite element shape functions in the level of resolution (i.e., a relatively small number is used in describing the inelastic strain and stress fields) as well as continuity (chosen to be $C^{-1}(\Theta)$ continuous, consistent with the strain and stress continuity in finite elements). The shape functions are taken to satisfy the partition of unity property ($\sum_{\alpha=1}^{N}N^{(\alpha)}(\mathbf{y})=1$). The nonlocal weight functions, $\psi^{(\alpha)}$, satisfy positivity and normality, as well as orthonormality with the shape functions:

$$\psi^{(\alpha)}(\mathbf{y})\geq 0;\quad \int_{\Theta}\psi^{(\alpha)}(\mathbf{y})\,\mathrm{d}\mathbf{y}=1;\int_{\Theta}\psi^{(\alpha)}(\mathbf{y})N^{(\beta)}(\mathbf{y})\,\mathrm{d}\mathbf{y}=\delta^{(\alpha\beta)} \tag{53}$$

where, $\delta^{(\alpha\beta)}$ denotes the Kronecker delta (i.e., $\delta^{(\alpha\beta)}=1$ if $\alpha=\beta$; $\delta^{(\alpha\beta)}=0$ if $\alpha\neq\beta$). The orthonormality condition ensures the consistency of the reduced order discretization (i.e., Eqs. (49) and (50)) with the nonlocal averaging (i.e., Eqs. (51) and (52)) and can be verified by premultiplying Eqs. (49) and (50) with $\psi^{(\alpha)}$ and integrating over the RVE domain.

Substituting Eq. (49) into Eq. (47), premultiplying the resulting equation with $\psi^{(\alpha)}$ integrating over the RVE domain and taking a time derivative yields:

$$\dot{\varepsilon}_{ij}^{(\beta)}(\mathbf{x},t)-\sum_{\alpha=1}^{n}P_{ijkl}^{(\alpha\beta)}\dot{\mu}_{kl}^{(\alpha)}(\mathbf{x},t)=A_{ijkl}^{(\beta)}\dot{\bar{\varepsilon}}_{kl}(\mathbf{x},t) \tag{54}$$

in which, $\mathbf{P}^{(\alpha\beta)}$ and $\mathbf{A}^{(\beta)}$ are coefficient tensors expressed as a function of the influence functions as:

$$P_{ijkl}^{(\alpha\beta)}=\int_{\Theta}\int_{\Theta}\psi^{(\beta)}(\mathbf{y})N^{(\alpha)}(\hat{\mathbf{y}})g_{ijkl}(\mathbf{y},\hat{\mathbf{y}})\,\mathrm{d}\hat{\mathbf{y}}\,\mathrm{d}\mathbf{y} \tag{55}$$

$$A_{ijkl}^{(\beta)}=\int_{\Theta}\psi^{(\beta)}(\mathbf{y})A_{ijkl}(\mathbf{y})\,\mathrm{d}\mathbf{y} \tag{56}$$

and,

$$\epsilon_{ij}^{(\alpha)}(\mathbf{x},t)\coloneqq\int_{\Theta}\psi^{(\alpha)}(\mathbf{y})\epsilon_{ij}^{0}(\mathbf{x},\mathbf{y},t)\,\mathrm{d}\mathbf{y} \tag{57}$$

is the nonlocal strain coefficient.

Considering the O(1) constitutive equation (i.e., Eq. (20) with $a = 0$), premultiplying by $\psi^{(\alpha)}$, integrating over the RVE domain and taking the time derivative results in:

$$\dot{\varepsilon}_{ij}^{(\beta)}(\mathbf{x},t) = \dot{\mu}_{ij}^{(\beta)}(\mathbf{x},t) + \sum_{\alpha=1}^{n} M_{ijkl}^{(\alpha\beta)} \dot{\sigma}_{kl}^{(\alpha)}(\mathbf{x},t) \tag{58}$$

where, $\mathbf{M}^{(\alpha\beta)}$ is expressed as:

$$M_{ijkl}^{(\alpha\beta)} = \int_{\Theta} \psi^{(\beta)}(\mathbf{y}) M_{ijkl}(\mathbf{y}) N^{(\alpha)}(\mathbf{y})\, \mathrm{d}\mathbf{y} \tag{59}$$

in which, $\mathbf{M}$ is the elastic compliance tensor. Combining Eqs. (54) and (58):

$$\sum_{\alpha=1}^{n} M_{ijkl}^{(\alpha\beta)} \dot{\sigma}_{kl}^{(\alpha)}(\mathbf{x},t) - \sum_{\alpha=1}^{n} \left[P_{ijkl}^{(\alpha\beta)} - \delta^{(\alpha\beta)} I_{ijkl}\right] \dot{\mu}_{kl}^{(\alpha)}(\mathbf{x},t) = A_{ijkl}^{(\beta)} \dot{\bar{\varepsilon}}_{kl}(\mathbf{x},t) \tag{60}$$

Equation (60) along with evolution equations for the eigenstrain coefficients $\mu^{(\alpha)}$ (formulated below) could be evaluated to obtain the microstructure deformation state for a prescribed macroscale strain increment. The macroscale stress is then computed by averaging Eq. (50) over the domain of the RVE.

Clearly, the number and form of the shape functions employed in the reduced order discretization of the eigenstrain and stress fields affect the accuracy and efficiency of the resulting model order. It is possible to prescribe piecewise constant or nonuniform variations for the shape functions [47, 51, 44]. In this work, piecewise constant shape functions are employed, which allows achieving evolution functions for the eigenstrain coefficients without further assumptions.

Considering the partitioning of the RVE domain into $n \geq n_{grain}$ nonoverlapping subdomains denoted by $\Theta^{(\alpha)}$ (i.e., $\Theta = \cup_{\alpha=1}^{n} \Theta^{(\alpha)}$ and $\Theta^{(\alpha)} \cap \Theta^{(\beta)} = \emptyset$ for $\alpha \neq \beta$). The partitioning is performed such that each subdomain is allowed to occupy the whole or a part of a single grain within the RVE only (i.e., $\Theta^{(\alpha)} \subseteq \Theta_{gr}^{(i)}$, $1 \leq i \leq n_{grain}$, $\forall \alpha \in \{1, 2, ..., n\}$). The shape and weighting functions are then chosen as:

$$N^{(\alpha)}(\mathbf{y}) = \begin{cases} 1 & \mathbf{y} \in \Theta^{(\alpha)} \\ 0 & \mathbf{y} \notin \Theta^{(\alpha)} \end{cases} \quad ; \quad \psi^{(\alpha)}(\mathbf{y}) = \frac{1}{|\Theta^{(\alpha)}|} N^{(\alpha)}(\mathbf{y}) \tag{61}$$

It is trivial to see that Eq. (61) satisfy the partition of unity, positivity, normality and orthonormality properties defined above.

Premultiplying the O(1) evolution laws for the inelastic strain, and the resolved shear stress (Eqs. (28) and (23), respectively with $a = 0$), and averaging over the domain of the RVE yields:

$$\dot{\mu}_{ij}^{(\alpha)}(\mathbf{x},t) = \sum_{s=1}^{N} \int_{\Theta} \psi^{(\alpha)}(\mathbf{y}) \dot{\gamma}^{s,0}(\mathbf{x},\mathbf{y},t) Z_{ij}^{s}(\mathbf{y})\, \mathrm{d}\mathbf{y} \tag{62}$$

$$\tau^{s(\alpha)}(\mathbf{x},t) = \sigma_{ij}^{(\alpha)}(\mathbf{x},t) Z_{ij}^{s(\alpha)} \tag{63}$$

where $\dot{\gamma}^{s(\alpha)}$ and $\tau^{s(\alpha)}$ are the part average of the slip rate and resolved shear stress of the s^{th} slip system, respectively (i.e., $\dot{\gamma}^{s(\alpha)} = \langle \dot{\gamma}^{s,0} \rangle_{\Theta^\alpha}$ and $\tau^{s(\alpha)} = \langle \tau^{s,0} \rangle_{\Theta^\alpha}$). $\tau^{s(\alpha)}$ denotes the Schmid tensor associated with the grain that contains $\Theta^{(\alpha)}$.

The O(1) evolution of the viscoplastic slip and slip strength (Eqs. (26) and (30)) are described by the ordinary differential equations as a function of the resolved shear stress. In the general form:

$$\dot{\gamma}^{s,0} = \dot{\gamma}\big(\gamma^{s,0}, \tau^{s,0}\big) \tag{64}$$

$$\dot{g}^{s,0} = \dot{g}\big(g^{s,0}, \tau^{s,0}\big) \tag{65}$$

Noting that the resolved shear stress in the reduced order model is piecewise uniform by the above arguments (i.e., $\tau^{s,0} = \tau^{s(\alpha)}$ when $y \in \Theta^{(\alpha)}$), considering that the slip and hardening evolve from a uniform reference state, the slip and hardening will evolve as piecewise uniform, which is described using the part averaged counterparts as :

$$\dot{\gamma}^{s(\alpha)}(\mathbf{x},t) = \dot{\gamma}_0 \left(\frac{\big|\tau^{s(\alpha)}(\mathbf{x},t)\big|}{g^{s(\alpha)}(\mathbf{x},t)} \right)^{1/m} \operatorname{sgn}\big(\tau^{s(\alpha)}(\mathbf{x},t)\big) \tag{66}$$

$$\dot{g}^{s(\alpha)}(\mathbf{x},t) = h_0 \left(\frac{g_{sa}^{s(\alpha)} - g^{s(\alpha)}(\mathbf{x},t)}{g_{sa}^{s(\alpha)} - g_0^{s(\alpha)}} \right) \sum_{s=1}^{N} |\dot{\gamma}^{s(\alpha)}(\mathbf{x},t)| \tag{67}$$

Box 3 summarizes the reduced order microscale problem, which replaces the numerical evaluation of the system described in Box 2. The overall order (i.e., the size of the linear systems evaluated in the context of the nonlinear solver) is $6n$ for a 3-D microstructure, where the unknowns are the nonlocal stress coefficients at each part, Θ^α, while the hardening coefficients evaluated explicitly, as described in Section 5.

4.1 Influence functions

The coefficient tensors $\mathbf{A}^{(\alpha)}$ and $\mathbf{P}^{(\alpha\beta)}$ used in the reduced order model are functions of the elastic (i.e., $\mathbf{H}(\mathbf{y})$) and eigenstrain (i.e., $\mathbf{h}(\mathbf{y},\hat{\mathbf{y}})$) influence functions, respectively. Furthermore, $\mathbf{A}^{(\alpha)}$ and $\mathbf{P}^{(\alpha\beta)}$ inherit minor symmetry from $\mathbf{G}(\mathbf{y})$ and $\mathbf{g}(\mathbf{y},\hat{\mathbf{y}})$.

Considering the microscale equilibrium defined in Eq. (44) in the absence of any inelastic strains:

$$\{L_{ijmn}(\mathbf{y})[H_{(m,y_n)kl}(\mathbf{y}) + I_{mnkl}]\}_{,y_j} = 0; \qquad \mathbf{y} \in \Theta \tag{68}$$

is the governing equation for evaluating the elastic influence function. Equation (68) is the classical influence function problem of linear elastic mathematical homogenization theory [4]

Given: part-wise parameters $M^{(\beta)}_{ijkl}$, $P^{(\alpha\beta)}_{ijkl}$, $A^{(\beta)}_{ijkl}$, $\mathbf{n}^{s(\alpha)}$, $\mathbf{m}^{s(\alpha)}$, $g^{s(\alpha)}_{sa}$, $\dot{\gamma}^{s(\alpha)}_0$, $h^{(\alpha)}_0$, $g^{s(\alpha)}_{s0}$, $\dot{\gamma}^{(\alpha)}_{s0}$, the macroscale strain $\bar{\varepsilon}_{kl}$ with its increment $\Delta\bar{\varepsilon}_{kl}$

Find: macroscale stress $\bar{\sigma}_{kl}$

- Constitutive equation:

$$\sum_{\alpha=1}^{n} M^{(\alpha\beta)}_{ijkl}\dot{\sigma}^{(\alpha)}_{kl}(\mathbf{x},t) - \sum_{\alpha=1}^{n}\left[P^{(\alpha\beta)}_{ijkl} - \delta^{(\alpha\beta)}I_{ijkl}\right]\dot{\mu}^{(\alpha)}_{kl}(\mathbf{x},t) = A^{(\beta)}_{ijkl}\dot{\bar{\varepsilon}}_{kl}(\mathbf{x},t)$$

$$\bar{\sigma}_{ij} = \sum_{\beta=1}^{n}\frac{|\Theta^{(\beta)}|}{|\Theta|}\sigma^{(\beta)}_{ij}$$

- Kinematics:

$$\dot{\mu}^{(\alpha)}_{ij}(\mathbf{x},t) = \sum_{s=1}^{N}\dot{\gamma}^{s(\alpha)}(\mathbf{x},t)\, Z^{s(\alpha)}_{ij}$$

- Flow rule:

$$\dot{\gamma}^{s(\alpha)}(\mathbf{x},t) = \dot{\gamma}_0\left(\frac{\left|\tau^{s(\alpha)}(\mathbf{x},t)\right|}{g^{s(\alpha)}(\mathbf{x},t)}\right)^{1/m}\operatorname{sgn}\left(\tau^{s(\alpha)}(\mathbf{x},t)\right)$$

- Hardening rule:

$$\dot{g}^{s(\alpha)}(\mathbf{x},t) = h_0\left(\frac{g^{s(\alpha)}_{sa} - g^{s(\alpha)}(\mathbf{x},t)}{g^{s(\alpha)}_{sa} - g^{s(\alpha)}_0}\right)\sum_{s=1}^{N}|\dot{\gamma}^{s(\alpha)}(\mathbf{x},t)|$$

- Schmid's law:

$$\tau^{s(\alpha)}(\mathbf{x},t) = \boldsymbol{\sigma}^{(\alpha)}(\mathbf{x},t) : \boldsymbol{Z}^{s(\alpha)} \qquad \boldsymbol{Z}^{s(\alpha)} = \mathbf{n}^{s(\alpha)}\otimes\mathbf{m}^{s(\alpha)}$$

Box 3: Reduced order microscale problem.

and is well-posed up to rigid body motion when periodicity condition is enforced along the RVE boundaries.

Substituting the eigenstrain discretization (Eq. (49)) and (Eq. (68)) into Eq. (44) and observing that the nonlocal eigenstrain coefficients is a function of the macroscale spatial coordinates only:

$$\left\{L_{ijmn}(\mathbf{y})\left[h^{(\alpha)}_{(m,y_n)kl}(\mathbf{y},\hat{\mathbf{y}}) - I_{mnkl}N^{(\alpha)}(\mathbf{y})\right]\right\}_{,y_j} = 0; \quad \mathbf{y}\in\Theta \tag{69}$$

is the governing equation for evaluating the part-wise eigenstrain influence function, $\mathbf{h}^{(\alpha)}$. Equation (69) is also well-posed up to rigid body motion when periodicity is imposed along the RVE boundary. It is possible to evaluate $\mathbf{P}^{(\alpha\beta)}$ directly using the part-wise eigenstrain influence functions as:

$$P^{(\alpha\beta)}_{ijkl} = \int_{\Theta}\psi^{(\beta)}(\mathbf{y})h^{(\alpha)}_{(i,y_j)kl}(\mathbf{y},\hat{\mathbf{y}})\,\mathrm{d}\mathbf{y} \tag{70}$$

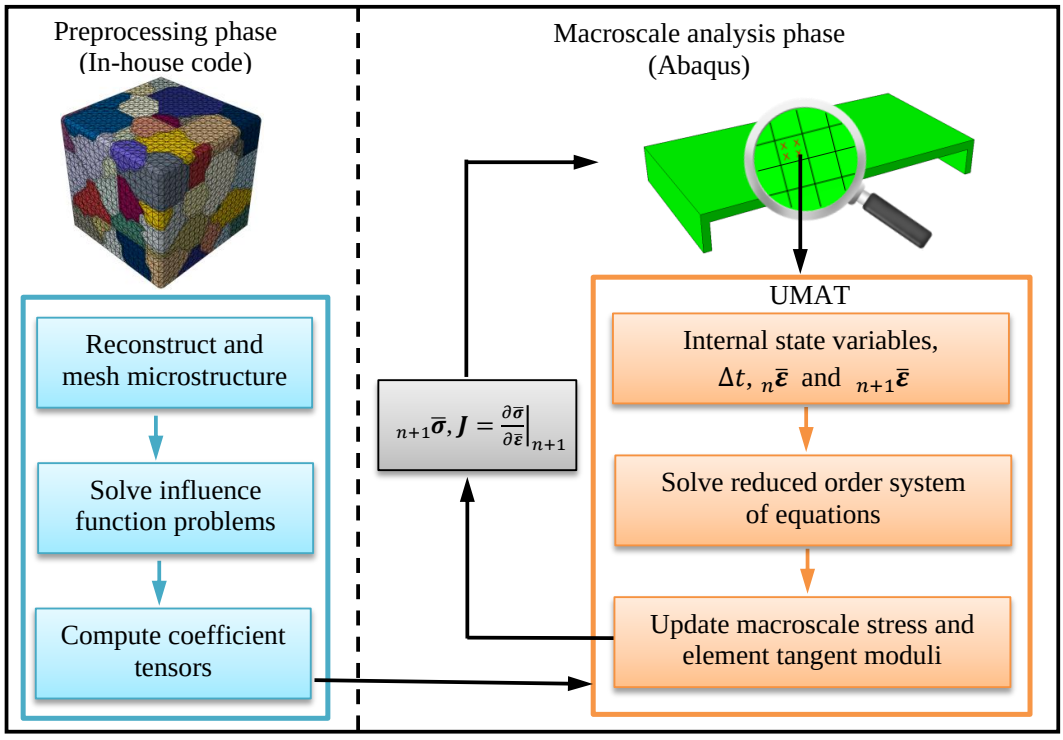

Figure 3: Implementation strategy for the reduced order multiscale model.

The evaluation of the eigenstrain influence function itself, which is costly from computational and memory standpoints, is therefore not necessary to evaluate coefficient tensors.

5 Computational implementation

The proposed reduced order polycrystal plasticity model has been implemented and the implementation details are provided in this section. The overview of the implementation strategy is shown in Fig. 3. The evaluation of the multiscale problem is performed in two stages. The preprocessing stage consists of the generation of the RVE and the evaluation of the coefficient tensors. The simulation of the macroscale problem (Box 1) is performed using the commercial finite element analysis package, Abaqus. The evaluation of the reduced order microstructure (Box 3) that constitutes the stress update of the macroscale analysis is incorporated as a user supplied subroutine (i.e., UMAT). In the context of the assumed strain approach, the reduced order model evaluates the reduced order microstructure problem and computes the macroscale stress and tangent stiffness matrix from a given equilibrium state and strain increment at a macroscale quadrature point as described below. In this section, we particularly focus on the evolution of the part-wise eigenstrain influence functions and the update procedure for the reduced order model.

5.1 Evaluation of the influence functions

The elastic and part-wise eigenstrain influence functions are numerically evaluated using the finite element method by solving Eqs. (68) and (69), respectively. The evaluation of elastic influence functions are standard (see, e.g., [27]) and skipped here for brevity.

Substituting the choice of the reduced order model shape functions into the eigenstrain influence function problem (69) and bringing the resulting equation into the weak form using the standard Bubnov-Galerkin procedure:

$$\int_{\Theta} w_{(i,y_j)}(\mathbf{y}) L_{ijmn}(\mathbf{y}) h^{(\alpha)}_{(m,y_n)kl}(\mathbf{y},\hat{\mathbf{y}})\,\mathrm{d}\mathbf{y} = \int_{\Theta^{(\alpha)}} w_{(i,y_j)}(\mathbf{y}) L_{ijkl}(\mathbf{y})\,\mathrm{d}\mathbf{y}; \quad \alpha = 1,2,...,n \tag{71}$$

where $w(\mathbf{y}) \in \mathcal{W}_{\mathrm{per}} \subset \left[H^1_{\mathrm{per}}(\Theta)\right]^{n_{\mathrm{sd}}}$ is the weight function with sufficient smoothness over the domain of the RVE, $H^1_{\mathrm{per}}(\Theta)$ denotes the Sobolev space of Θ-periodic functions with square integrable values and derivatives defined within the problem domain, Θ. The space of the weight functions and the test functions are taken to be finite dimensional subspaces discretized using the standard finite element shape functions. Following the finite element discretization and assembly procedure, the resulting series of linear systems for the evaluation of the part-wise inelastic influence function becomes:

$$\mathbf{K}\mathbf{d}^{(\alpha)}_K = \mathbf{F}^{(\alpha)}_K; \quad \alpha = 1,2,\ldots,n;\ K = 1,2,\ldots,6 \tag{72}$$

where, $\mathbf{K}$ denotes the stiffness matrix, $\mathbf{F}^{(\alpha)}_K$ and $\mathbf{d}^{(\alpha)}_K$ denote the force vector and the nodal coefficient vector for the K^{th} component of the α^{th} influence function, respectively. Voigt notation is employed to condense the indices (i.e., $ij \rightarrow K$ with $11 \rightarrow 1$, $22 \rightarrow 2$, $33 \rightarrow 3$, $23 \rightarrow 4$, $13 \rightarrow 5$, $12 \rightarrow 6$) and K condenses the free indices in Eq. (69). It is important to note that the stiffness matrix, $\mathbf{K}$, is identical for all eigenstrain influence functions and therefore require a single factorization. $\mathbf{d}^{(\alpha)}_K$ denotes the nodal coefficient of the part-wise influence function of α^{th} part and $\mathbf{F}^{(\alpha)}_K$ denotes the corresponding force vector. Figure 4 schematically indicates the part-wise influence function problem, where the RVE subdomain associated with part α is subjected to a spatially uniform body force as expressed on the right-hand side of Eq. (71).

Representative polycrystal microstructures are generated using the DREAM.3D software [18], which is capable of creating synthetic RVEs based on microstructure topology metrics such as grain size, orientation and misorientation distributions or reconstruct microstructure directly from sectioned images of real microstructures. The geometry generated with DREAM.3D is discretized using the Parallelized Polycrystal Mesher developed by Cerrone et al. [6]. Figure 5 demonstrates the geometry and discretization of a representative microstructure.

The real or reconstructed polycrystal microstructures are often at best close to but not strictly periodic. In strictly periodic microstructure, the periodicity of the influence functions can be enforced by matching the surface nodes along the opposing sides of the RVE, assigning master-slave pairs and constraining the deformation of slave nodes to the deformation of the

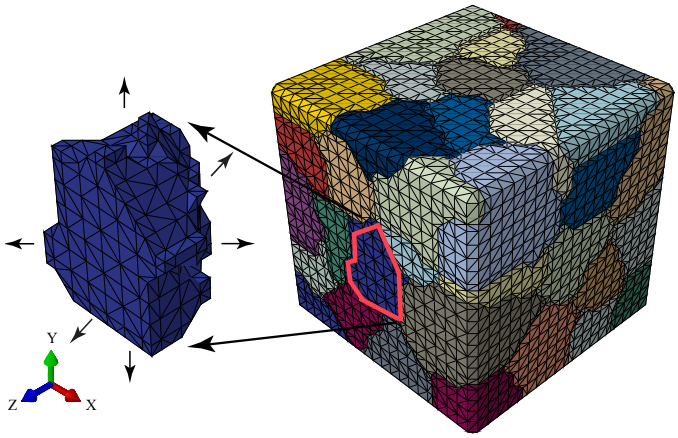

Figure 4: Solving influence functions part-by-part (using entire grain as one part as an example).

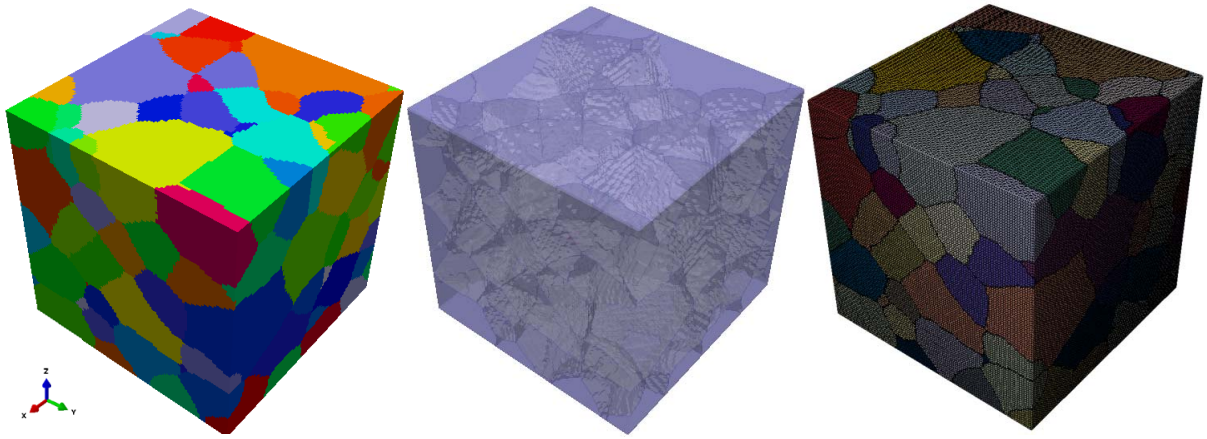

(a) (b) (c)

Figure 5: A virtual micro-structure generated from DREAM.3D and Meshed with PPM: (a) synthetic poly-crystal micro-structure; (b) internal grain boundaries based on which meshing of individual grain is conducted; (c) volume mesh.

corresponding master nodes, which is not applicable in polycrystal RVEs. Nguyen et al. [48] proposed interpolating the displacement of two opposite RVE faces by linear combinations of polynomial shape functions for nonmatching RVE mesh. We rely on a similar idea combined with the classic master-slave coupling method to enforce a quasi-periodicity to provide point-wise displacement matching between opposing RVE surfaces with nonmatching meshes. Consider the discretization of the RVE using four-noded tetrahedra. The general treatment of the quasi-periodic mesh applies to hexahedra in a straight forward manner as well. The opposing external surfaces of the RVE are designated as master and slave surfaces. In case of uneven mesh density, slave surface is chosen to be that with the finer mesh density. The

system of equations (Eq. (72)) is rearranged in the following form:

$$\begin{bmatrix} \boldsymbol{K}_{ii} & \boldsymbol{K}_{im} & \boldsymbol{K}_{is} & \boldsymbol{K}_{if} \\ \boldsymbol{K}_{mi} & \boldsymbol{K}_{mm} & \boldsymbol{K}_{ms} & \boldsymbol{K}_{mf} \\ \boldsymbol{K}_{si} & \boldsymbol{K}_{sm} & \boldsymbol{K}_{ss} & \boldsymbol{K}_{sf} \\ \boldsymbol{K}_{fi} & \boldsymbol{K}_{fm} & \boldsymbol{K}_{fs} & \boldsymbol{K}_{ff} \end{bmatrix} \begin{Bmatrix} \boldsymbol{d}^i \\ \boldsymbol{d}^m \\ \boldsymbol{d}^s \\ \boldsymbol{d}^f \end{Bmatrix} = \begin{Bmatrix} \boldsymbol{F}_1 \\ \boldsymbol{F}_2 \\ \boldsymbol{F}_3 \\ \boldsymbol{F}_4 \end{Bmatrix} \tag{73}$$

where $\mathbf{d}^i$, $\mathbf{d}^m$, $\mathbf{d}^s$ and $\mathbf{d}^f$ respectively denote the displacement vector that correspond to the interior, master, slave and fixed nodes respectively. The part and component indicators from the displacement vectors (Eq. (72)) are omitted in Eq. (73) for simplicity. Due to the symmetry of the stiffness matrix, different components of the stiffness matrix satisfy:

$$\boldsymbol{K}_{pq} = \boldsymbol{K}_{qp}^T \; ; \quad p \in \{i, m, s, f\}, q \in \{i, m, s, f\} \tag{74}$$

The corner nodes of the RVE are fixed to prevent rigid body motion, which implies:

$$\boldsymbol{d}^f = \mathbf{0} \tag{75}$$

Every node on the slave surface is associated with a dummy master node, which is a projection of the slave node onto the master surface as illustrated in Fig. 6(a). The dummy master node lies on the face, edge or a vertex of a dummy master element as illustrated in Fig. 6(b). The displacement of the slave node is expressed as:

$$\mathbf{d}_b = \sum_{p=1}^{4} N_p^e(\hat{\mathbf{y}}_b)\mathbf{d}_p^e \tag{76}$$

where $\mathbf{d}_b$ denotes the displacement vector of the slave node, b, $\hat{\mathbf{y}}_b$ denotes the coordinates of the dummy master node, $\mathbf{d}^e$ and $\mathbf{N}^e$ denote the local displacement vector and finite element shape functions of the nodes in the dummy master element, e, respectively. Applying Eq. (76) to all nodes on slave surfaces of the RVE boundaries, yields the relationship between the slave and master displacement vectors as:

$$\boldsymbol{d}^s = \mathbf{C}\boldsymbol{d}^m \tag{77}$$

in which $\mathbf{C}$ is a rectangular matrix that contains the corresponding coefficients from Eq. (76).

Lagrange multipliers are used to enforce the boundary constraints. Consider the Lagrangian:

$$\Pi(\boldsymbol{d}) = \frac{1}{2}\boldsymbol{d}^T\boldsymbol{K}\boldsymbol{d} - \boldsymbol{d}^T\boldsymbol{F} + \boldsymbol{\lambda}_1^T(\boldsymbol{d}^s - \boldsymbol{C}\boldsymbol{d}^m) + \boldsymbol{\lambda}_2^T\boldsymbol{d}^f \tag{78}$$

in which, $\boldsymbol{\lambda}_1^T$ and $\boldsymbol{\lambda}_2^T$ are two Lagrange multipliers ensuring the enforcement of the periodic boundary conditions on the RVE boundaries (Eq. (77)) and fixed boundary conditions on the corner nodes (Eq. (75)). Taking derivative of Π with respect to $\boldsymbol{d}^i$, $\boldsymbol{d}^m$, and $\boldsymbol{d}^s$, and

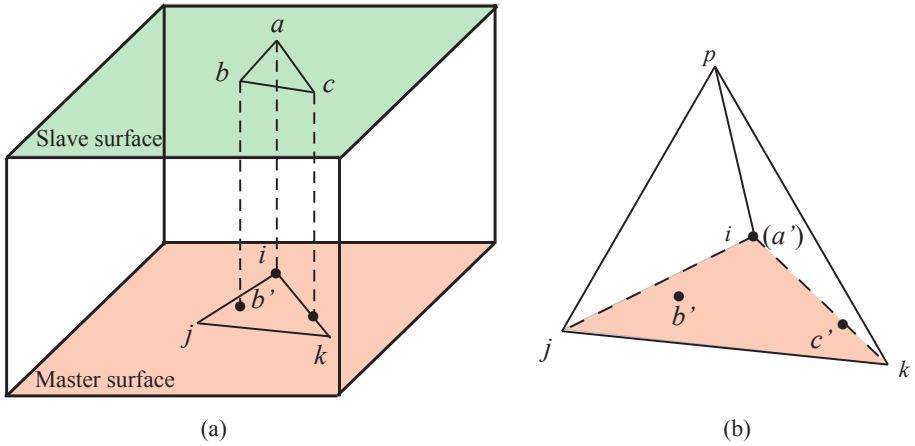

Figure 6: Master-Slave relationship for non-periodic mesh RVE.

incorporating Eqs. (75) and (74) gives:

$$\boldsymbol{K}_{ii}\boldsymbol{d}^{i} + \boldsymbol{K}_{im}\boldsymbol{d}^{m} + \boldsymbol{K}_{is}\boldsymbol{d}^{s} - \boldsymbol{F}_{1} = \boldsymbol{0} \tag{79}$$

$$\boldsymbol{K}_{mi}\boldsymbol{d}^{i} + \boldsymbol{K}_{mm}\boldsymbol{d}^{m} + \boldsymbol{K}_{ms}\boldsymbol{d}^{s} - \boldsymbol{F}_{2} - \boldsymbol{C}^{T}\boldsymbol{\lambda}_{1} = \boldsymbol{0} \tag{80}$$

$$\boldsymbol{K}_{si}\boldsymbol{d}^{i} + \boldsymbol{K}_{sm}\boldsymbol{d}^{m} + \boldsymbol{K}_{ss}\boldsymbol{d}^{s} - \boldsymbol{F}_{3} + \boldsymbol{\lambda}_{1} = \boldsymbol{0} \tag{81}$$

Premultiplying Eq. (81) with $\mathbf{C}^T$, adding with Eq. (80) and considering the periodic boundary condition in Eq. (77), yields:

$$\Big(\boldsymbol{K}^{mi} + \boldsymbol{C}^{T}\boldsymbol{K}_{si}\Big)\boldsymbol{d}_{i} + \Big(\boldsymbol{K}_{mm} + \boldsymbol{C}^{T}\boldsymbol{K}_{sm} + \boldsymbol{K}_{ms}\boldsymbol{C} + \boldsymbol{C}^{T}\boldsymbol{K}_{ss}\boldsymbol{C}\Big)d^{m} - \boldsymbol{F}_{2} - \boldsymbol{C}^{T}\boldsymbol{F}_{3} = \boldsymbol{0} \tag{82}$$

Substituting Eq. (77) into Eq. (79) and combining with Eq. (82) gives:

$$\begin{bmatrix} \boldsymbol{K}_{ii} & \boldsymbol{K}_{im} + \boldsymbol{K}_{is}\boldsymbol{C} \\ \boldsymbol{K}_{mi} + \boldsymbol{C}^{T}\boldsymbol{K}_{si} & \boldsymbol{K}_{mm} + \boldsymbol{C}^{T}\boldsymbol{K}_{sm} + \boldsymbol{K}_{ms}\boldsymbol{C} + \boldsymbol{C}^{T}\boldsymbol{K}_{ss}\boldsymbol{C} \end{bmatrix} \begin{Bmatrix} \boldsymbol{d}^{i} \\ \boldsymbol{d}^{m} \end{Bmatrix} = \begin{Bmatrix} \boldsymbol{F}_{1} \\ \boldsymbol{F}_{2} + \boldsymbol{C}^{T}\boldsymbol{F}_{3} \end{Bmatrix} \tag{83}$$

The condensed stiffness matrix in Eq. (83) is used to solve for the interior and master nodal coordinates. The slave nodal coordinates, $\mathbf{d}^s$, is then computed using Eq. (77). It is straightforward to see that the symmetry of the stiffness matrix has been preserved. Equation (83) is evaluated for each part for a total of n times.

5.2 Evaluation of the reduced order microscale problem

The reduced order system of equations in Box 3 is solved numerically at each macroscale quadrature point to incrementally update the macroscale stress from an equilibrium state for a given increment of macroscopic strain.

The reduced order system is viewed as two sets of coupled nonlinear equations (i.e., the constitutive equations and hardening rules) with $\boldsymbol{\sigma}^{(\beta)}$ and $g^{s(\beta)}$ ($\beta = 1, 2, ..., n$, $s = 1, 2, ..., N$)

as unknowns, which can be written in the vectorized form as:

$$\boldsymbol{\Sigma} = \left(\sigma_1^{(1)}, \sigma_2^{(1)}, \dots, \sigma_6^{(1)}, \sigma_1^{(2)}, \dots, \sigma_6^{(2)}, \dots, \sigma_1^{(n)}, \dots, \sigma_6^{(n)}\right)^T \tag{84}$$

$$\boldsymbol{G} = \left(g^{1(1)}, g^{2(1)}, \dots, g^{N(1)}, g^{1(2)}, \dots, g^{N(2)}, \dots, g^{1(n)}, \dots, g^{N(n)}\right)^T \tag{85}$$

A full tight coupled Newton-Raphson (N-R) method [42] or a two-level staggering scheme [39] could be used to solve the reduced order microscale problem. In this manuscript, a staggering scheme is adopted, in which the part-wise stresses and the part-wise strengths are evaluated in a coupled but iterative manner. While the convergence of the system is first order (as opposed to a tight coupled N-R scheme that has second order convergence), the generalization of the implementation of the approach to other evolution laws is somewhat more straightforward using the present formulation. The incremental procedure for evaluating the reduced order microscale problem is shown in Box 4.

Given: Stress and strength of each part at the l^{th} increment, ${}_{l}\boldsymbol{\Sigma}$ and ${}_{l}\boldsymbol{G}$; macroscale strain and strain increment, ${}_{l+1}\bar{\boldsymbol{\epsilon}}$ and ${}_{l+1}\Delta\bar{\boldsymbol{\epsilon}}$; time and time increment, ${}_{l}t$ and ${}_{l+1}\Delta t$.

Find: Stress and strength of each part at the $l+1^{th}$ increment, ${}_{l+1}\boldsymbol{\Sigma}$ and ${}_{l+1}\boldsymbol{G}$.

- (A) Set iteration number $k = 0$
- (B) Initial guess for stress and strength:

  $${}^{0}_{l+1}\boldsymbol{\Sigma} = {}_{l}\boldsymbol{\Sigma}\ ;\ {}^{0}_{l+1}\mathbf{G} = {}_{l}\mathbf{G}$$

- (C) Iterate k until convergence:

  1) Update the stress using N-R iteration

  $${}^{k+1}_{l+1}\boldsymbol{\Sigma} = {}^{k}_{l+1}\boldsymbol{\Sigma} - \left(\frac{\partial \boldsymbol{\Phi}}{\partial \boldsymbol{\Sigma}}\right)^{-1}\Bigg|_{({}^{k}_{l+1}\boldsymbol{\Sigma},\, {}^{k}_{l+1}\mathbf{G})} \boldsymbol{\Phi}\Big|_{({}^{k}_{l+1}\boldsymbol{\Sigma},\, {}^{k}_{l+1}\mathbf{G})}$$

  2) Update the strength explicitly:

  $${}^{k+1}_{l+1}\boldsymbol{G} = {}^{k}_{l+1}\boldsymbol{G} + \dot{\mathbf{G}}\Big|_{({}^{k+1}_{l+1}\boldsymbol{\Sigma},\, {}^{k}_{l+1}\mathbf{G})}\, {}_{l+1}\Delta t$$

  2) $k = k + 1$

Box 4: Algorithm for solving the reduced order microscale problem

To define the residual, we discretize the constitutive equation using a backward Euler scheme. Adopting the Voigt notation:

$$\boldsymbol{\Phi} = \left(\phi_1^{(1)}, \phi_2^{(1)}, \dots, \phi_6^{(1)}, \phi_1^{(2)}, \dots, \phi_6^{(2)}, \dots, \phi_1^{(n)}, \dots, \phi_6^{(n)}\right)^T = \mathbf{0} \tag{86}$$

where,

$$\phi_I^{(\beta)} = \sum_{\alpha=1}^{n} \left(\delta^{(\alpha\beta)} I_{IJ} - P_{IJ}^{(\alpha\beta)}\right)\, {}_{l+1}\dot{\mu}_J^{(\alpha)} + M_{IJ}^{(\beta)} \frac{{}_{l+1}\sigma_J^{(\beta)} - {}_{l}\sigma_J^{(\beta)}}{{}_{l+1}t - {}_{l}t} - A_{IJ}^{(\beta)} \frac{{}_{l+1}\bar{\epsilon}_J - {}_{l}\bar{\epsilon}_J}{{}_{l+1}t - {}_{l}t} = 0 \tag{87}$$

in which, left subscripts l and $l+1$ indicate the values of the fields at current and next increments, respectively, that correspond to times ${}_{l}t$ and ${}_{l+1}t$. The time increment is: ${}_{l+1}\Delta t = {}_{l+1}t - {}_{l}t$. The Jacobian matrix for the N-R method is expressed as:

$$\frac{\partial \mathbf{\Phi}}{\partial \mathbf{\Sigma}} = \begin{bmatrix} \frac{\partial \phi_1^{(1)}}{\partial \sigma_1^{(1)}} & \frac{\partial \phi_1^{(1)}}{\partial \sigma_2^{(1)}} & \cdots & \frac{\partial \phi_1^{(1)}}{\partial \sigma_6^{(1)}} & \frac{\partial \phi_1^{(1)}}{\partial \sigma_1^{(2)}} & \cdots & \frac{\partial \phi_1^{(1)}}{\partial \sigma_6^{(n)}} \\ \frac{\partial \phi_2^{(1)}}{\partial \sigma_1^{(1)}} & \frac{\partial \phi_2^{(1)}}{\partial \sigma_2^{(1)}} & \cdots & \frac{\partial \phi_2^{(1)}}{\partial \sigma_6^{(1)}} & \frac{\partial \phi_2^{(1)}}{\partial \sigma_1^{(2)}} & \cdots & \frac{\partial \phi_2^{(1)}}{\partial \sigma_6^{(n)}} \\ \vdots & \vdots & \cdots & \vdots & \ddots & \vdots & \\ \frac{\partial \phi_6^{(1)}}{\partial \sigma_1^{(1)}} & \frac{\partial \phi_6^{(1)}}{\partial \sigma_2^{(1)}} & \cdots & \frac{\partial \phi_6^{(1)}}{\partial \sigma_6^{(1)}} & \frac{\partial \phi_6^{(1)}}{\partial \sigma_1^{(2)}} & \cdots & \frac{\partial \phi_6^{(1)}}{\partial \sigma_6^{(n)}} \\ \frac{\partial \phi_1^{(2)}}{\partial \sigma_1^{(1)}} & \frac{\partial \phi_1^{(2)}}{\partial \sigma_2^{(1)}} & \cdots & \frac{\partial \phi_1^{(2)}}{\partial \sigma_6^{(1)}} & \frac{\partial \phi_1^{(2)}}{\partial \sigma_1^{(2)}} & \cdots & \frac{\partial \phi_1^{(2)}}{\partial \sigma_6^{(n)}} \\ \vdots & \vdots & \cdots & \vdots & \ddots & \vdots & \\ \frac{\partial \phi_6^{(n)}}{\partial \sigma_1^{(1)}} & \frac{\partial \phi_6^{(n)}}{\partial \sigma_2^{(1)}} & \cdots & \frac{\partial \phi_6^{(n)}}{\partial \sigma_6^{(1)}} & \frac{\partial \phi_6^{(n)}}{\partial \sigma_1^{(2)}} & \cdots & \frac{\partial \phi_6^{(n)}}{\partial \sigma_6^{(n)}} \end{bmatrix} \tag{88}$$

where each component is expressed as:

$$\frac{\partial \phi_I^{(\beta)}}{\partial \sigma_K^{(\eta)}} = \left(\delta^{(\eta\beta)} I_{IJ} - P_{IJ}^{(\eta\beta)}\right) \sum_{s=1}^{N} \Omega^{s(\eta)} Z_J^{s(\eta)} Z_K^{s(\eta)} + \delta^{(\eta\beta)} \frac{M_{IK}^{(\beta)}}{{}_{l+1}\Delta t} \tag{89}$$

and

$$\Omega^{s(\eta)} = \frac{\dot{\gamma}_0}{m} \frac{1}{g^{s(\eta)}} \left(\frac{|\tau^{s(\eta)}|}{g^{s(\eta)}}\right)^{\frac{1-m}{m}} \tag{90}$$

The incremental evaluation of the macroscale equilibrium is performed using the N-R method, in which the tangent moduli is:

$$\frac{\partial_{l+1}\bar{\sigma}_I}{\partial_{l+1}\bar{\epsilon}_J} = \sum_{\alpha=1}^{N} C^{(\alpha)} \frac{\partial_{l+1}\sigma_I^{(\alpha)}}{\partial_{l+1}\bar{\epsilon}_J} \tag{91}$$

where $C^{(\alpha)}$ is the volume fraction of part α. Eq. (91) indicates the need to calculate $\frac{\partial_{l+1}\sigma_I^{(\alpha)}}{\partial_{l+1}\bar{\epsilon}_J}$ to get the tangent moduli. This term is obtained by taking the derivative of Eq. (87) with respect to ${}_{l+1}\bar{\epsilon}_K$ and considering the chain rule:

$$\sum_{\alpha=1}^{n} \left(\delta^{(\alpha\beta)} I_{IJ} - P_{IJ}^{(\alpha\beta)}\right) \frac{\partial_{l+1}\dot{\mu}_J^{(\alpha)}}{\partial_{l+1}\tau^{s(\alpha)}} \frac{\partial_{l+1}\tau^{s(\alpha)}}{\partial_{l+1}\sigma_L^{(\alpha)}} \frac{\partial_{l+1}\sigma_L^{(\alpha)}}{\partial_{l+1}\bar{\epsilon}_K} + \frac{M_{IJ}^{(\beta)}}{{}_{l+1}\Delta t} \frac{\partial_{l+1}\sigma_J^{(\beta)}}{\partial_{l+1}\bar{\epsilon}_K} - \frac{A_{IJ}^{(\beta)}}{{}_{l+1}\Delta t} \frac{\partial_{l+1}\bar{\epsilon}_J}{\partial_{l+1}\bar{\epsilon}_K} = 0 \tag{92}$$

Simplifying the above equation yields:

$$\sum_{\alpha=1}^{n}\left[(\delta^{(\alpha\beta)}I_{IJ}-P_{IJ}^{(\alpha\beta)})\varphi_{JL}^{(\alpha)}+\delta^{(\alpha\beta)}M_{IL}^{(\alpha)}\right]\frac{\partial_{l+1}\sigma_L^{(\alpha)}}{\partial_{l+1}\bar{\epsilon}_K}=\frac{A_{IK}^{(\beta)}}{{}_{l+1}\Delta t} \tag{93}$$

where,

$$\varphi_{JL}^{(\alpha)}=\sum_{s=1}^{N}\frac{\dot{\gamma}_0}{m}\frac{1}{{}_{l+1}g^{s(\alpha)}}\left(\frac{\left|{}_{l+1}\tau^{s(\alpha)}\right|}{{}_{l+1}g^{s(\alpha)}}\right)^{\frac{1}{m}-1}Z_J^{s(\alpha)}Z_L^{s(\alpha)} \tag{94}$$

Equation (93) consists of a linear system of equations, from which $\frac{\partial_{l+1}\sigma_L^{(\alpha)}}{\partial_{l+1}\bar{\epsilon}_K}$ is calculated.

6 Numerical verification

The verification of the proposed reduced order homogenization based crystal plasticity model is performed using three sets of examples. The examples establish the accuracy characteristics of the proposed model as compared to the Crystal Plasticity Finite Element (CPFE) method, in which the microstructure is fully resolved. The first two sets of examples assess the accuracy and efficiency in the context of macroscopic metrics (e.g., homogenized stress-strain behavior) with the first set of example emphasizing on various loading conditions and the second set on different microstructure configurations. The third set of examples demonstrates the importance of employing subgrain partitioning when the local stress fields are of interest. A two-scale analysis of a circular arch subjected to compression is included in Section 6.4 to further demonstrated the computatonal capabilities of the proposed reduced order model.

Three polycrystalline microstructural configurations as shown in Fig. 7 are investigated during the verification process using the grain size distribution function shown in Fig. 8 and equiaxed grain shape. The rolling direction (RD) is along the X axis, while the transverse (TD) and the normal direction (ND) coincides with Y and Z, respectively. The polycrystalline microstructures are taken to consist of 52, 73 and 134 randomly oriented FCC grains of pure aluminum.

The finite element discretizations of the reference CPFE models are composed of trilinear four-noded tetrahedron elements. The three microstructures investigated contained 50,476, 69,291 and 94,409 elements that correspond to approximately 56,000, 76,000 and 103,000 degrees of freedom, respectively. The partitioning of the proposed reduced order models were performed such that each part coincides with a single grain (i.e., n=52, n =73 and n =134 for the three cases considered) leading to a nonlinear system with 312, 438 and 804 degrees of freedom, respectively. The macroscale discretization of the multiscale model consists of a single tri-linear eight-noded hexahedron element in the three sets of verification examples.

The properties of the material at the reference orientation (taken to be the same as the basis shown in Fig. 4) is summarized in Tables 1 and 2. All 12 $\{111\}\langle 111\rangle$ slip systems are taken to be active in the reference and multiscale simulations.

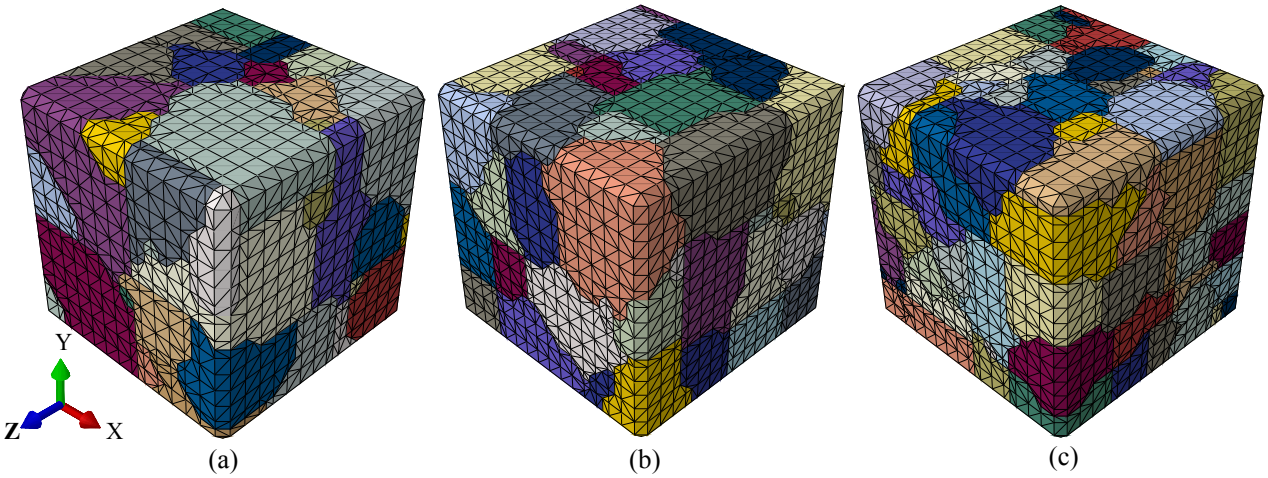

Figure 7: Three RVEs of different sizes: (a) small RVE with 52 grains; (b) medium RVE with 73 grains; (c) large RVE with 134 grains.

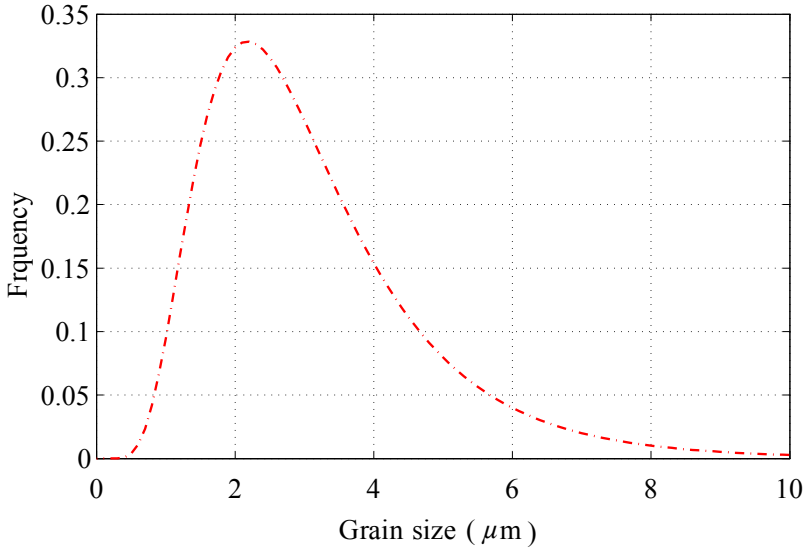

Figure 8: Grain size distribution function used in RVE microstructure generation.

Table 1: Elastic parameters.

C_{11} (GPa)	C_{12} (GPa)	C_{44} (GPa)
108.2	61.3	28.5

Table 2: Viscoplasticity parameters.

m	$\dot{\gamma}_0(s^{-1})$	h_0 (MPa)	g_0^s (MPa)	$g_{sa,0}^s$ (MPa)	m'	$\dot{\gamma}_{s0}(s^{-1})$
0.05	1.0	20.4	3.7	30.8	0.0	5.0×10^{10}

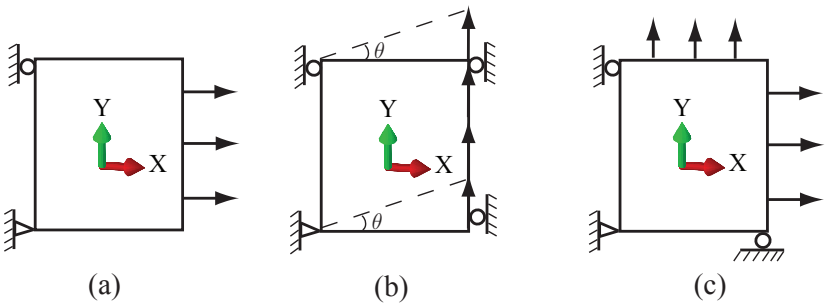

Figure 9: Schematic illustration of different boundary and loading conditions investigated: (a) unixial tension; (b)simple shear; (c)biaxial tension.

6.1 Effects of loading conditions

Uniaxial, simple shear and biaxial loading conditions are considered to investigate the performance of the ROM as shown in Fig. 9 (the illustration is in 2D for simplicity since no loadings are applied along the out-of-plane direction for all cases). Both monotonic and cyclic loading cases are studied under the biaxial tension conditions. For the uniaxial tension and simple shear, a 5% strain is applied with a constant strain rate of 0.05/s. For the monotonic biaxial tension case, a 5% strain is applied at a constant strain rate of 0.05/s along the X direction while a 3% strain is applied at a constant strain rate of 0.03/s along the Y direction. For the cyclic biaxial tension case, a 6% maximum strain is applied along the X direction with a constant strain rate of 0.04/s. Upon reaching the maximum strain, the loading is held until the end of the simulation. Along the Y direction, the microstructure is cyclically loaded with an R-ratio of one and applied strain range of 4% at constant strain rate 0.04/s. The duration of the cyclic biaxial tension simulation is 2.5 seconds.

Figure 10 shows the comparisons between overall stress-strain behaviors simulated using the proposed reduced order model and the reference model of the 73-grain RVE under above loading conditions with texture given in the {111} pole figure in Fig. 11. There is a reasonable overall match between the CPFE and the reduced order model behavior for all the loading conditions considered. The proposed model performed slightly stiffer than the reference simulation, which is expected because the proposed model employs a much reduced basis with uniform shape functions within each part. The model therefore does not capture strain/stress gradients within the part. Employing nonuniform shape functions [44, 45] or increasing the number of parts [51] may improve the accuracy.

6.2 Effects of microstructure configuration

For each microstructure in Fig. 7, 32 random grain orientation sets were generated in order to study the error characteristics of the proposed model as a function of the random microstructure geometry. Each microstructure is subjected to uniaxial tension along the X-direction up to 5% macroscopic strain with a strain rate of 0.05/s. All the 96 simulations show

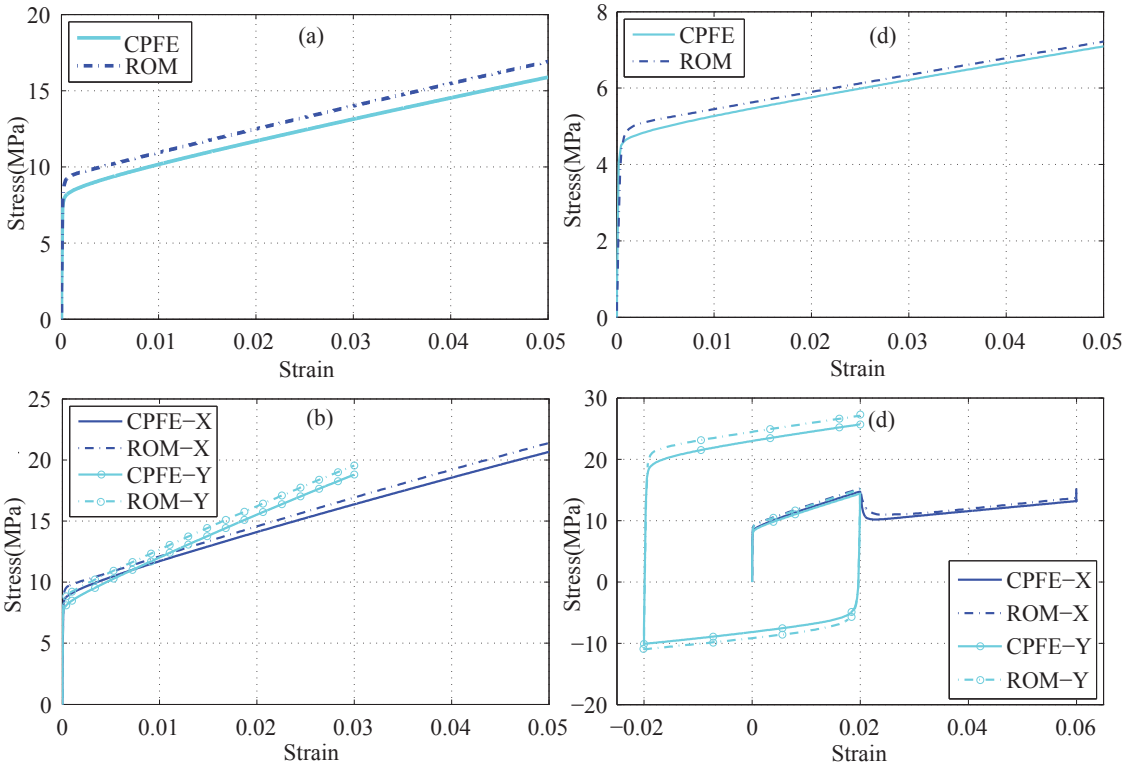

Figure 10: Overall constitutive behavior of the 73-grain RVE subjected to: (a) monotonic uniaxial tension; (b) monotonic simple shear; (c) monotonic biaxial tension; (d) cyclic biaxial tension.

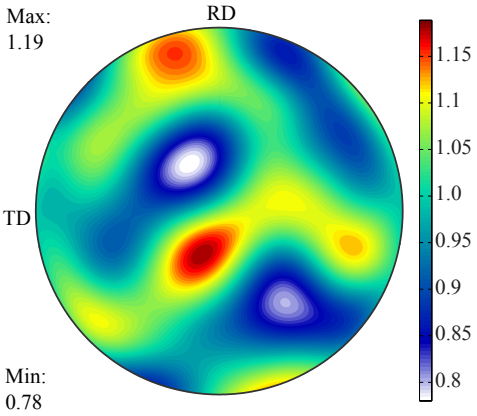

Figure 11: {111} pole figure of the initial texture of the 73-grain RVE.

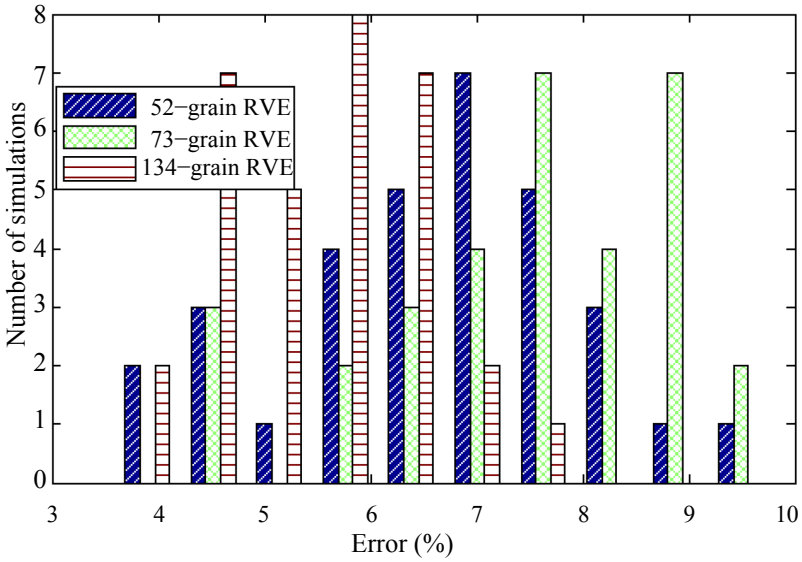

Figure 12: Overall stress approximation error distribution functions.

similar errors, and in order to give an overall description of the error of all the simulations, we define the overall stress approximation error as:

$$\text{error} = \int_0^{\epsilon} \frac{|\sigma_{\text{ROM}} - \sigma_{\text{CPFE}}|}{|\sigma_{\text{CPFE}}|} \, \mathrm{d}\epsilon \tag{95}$$

For the simulation shown in Fig. 10 (a), this error is calculated as 7.1%. The error distribution functions of the 96 simulations are shown in Fig. 12, which demonstrates that the error magnitude is quite stable across random realizations of orientation distributions, as well as microstructure morphologies.

Another RVE with elongated grains along X direction shown in Fig. 13) is used to evaluate ROM's performance when the grain shapes are not equiaxed and a preferred orientation exists. The same grain size distribution function is used as in Fig. 8 while the aspect ratio of RD/ND and RD/TD is set to 5.0 and 4.0, respectively, to enforce the elongated grain structure. This RVE consists of 62 grains and the initial texture is chosen such that it follows the pattern of the rolling texture of aluminum as reported in [40]. The $\{111\}\rangle$ pole figure of the initial texture is shown in Fig. 14. Figure 15 shows the overall constitutive behavior of this RVE subject to uniaxial tension along X and Z direction. ROM performs reasonably well along both loading directions, and, more importantly captures the anisotropic yielding and hardening effects in different loading directions caused by the microstructure anisotropy.

6.3 Effect of subgrain partitioning

The reduced order modeling approach, which includes one-part-per-grain partitioning, was demonstrated above to reasonably approximate the overall deformation behavior of the polycrystal. Often times, in addition to the overall constitutive response of the polycrystal, the

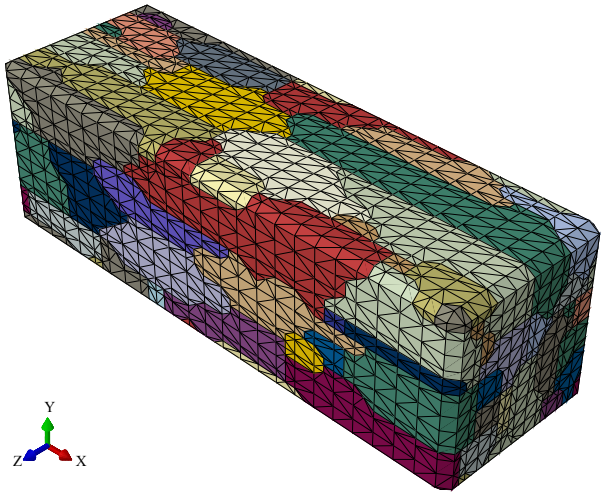

Figure 13: RVE with elongated grains along X direction

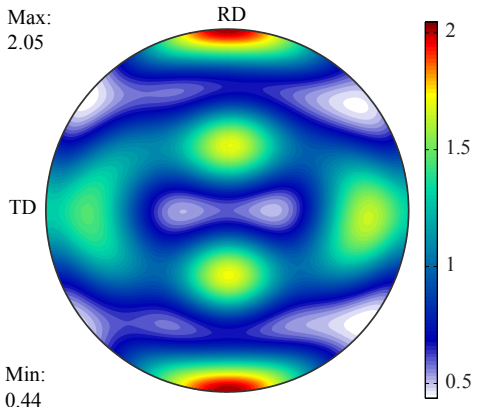

Figure 14: {111}) pole figure of the initial texture of the elongated RVE.

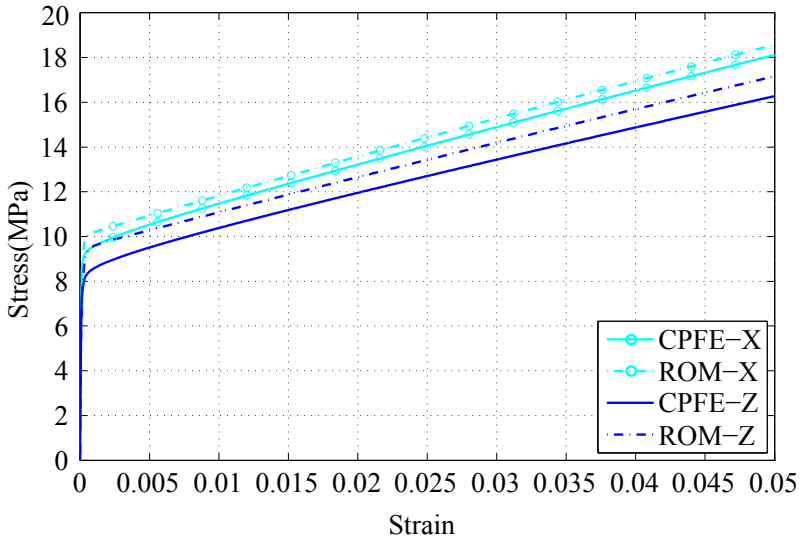

Figure 15: Overall constitutive behavior of a RVE with 62 elongated grains subject to uniaxial tension along different directions.

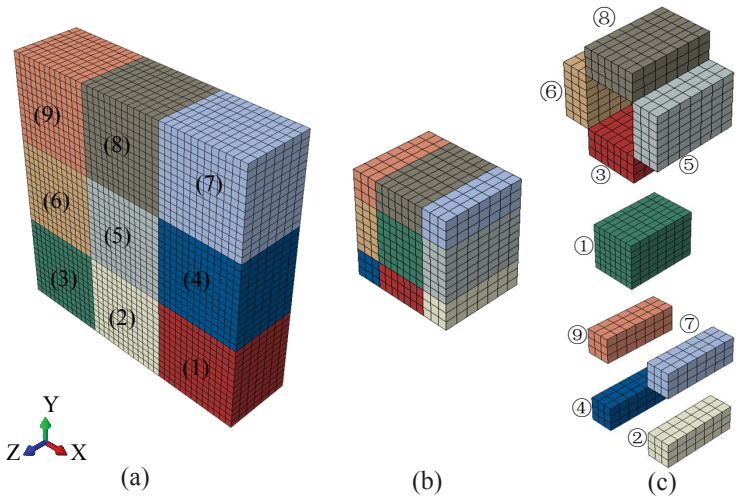

Figure 16: Sub-partitioning of the RVE: (a) RVE with grain ID; (b) sub-partitioning of grain No. 5; (c) parts in grain No.5 with part ID.

subgrain stress and strain concentrations are of significant concern. The accurate characterization of stresses along grain boundaries and triple junctions are critical to capturing the damage and crack initiation under fatigue and creep-fatigue loading. It is therefore of interest to demonstrate the capability of the proposed model in capturing the stresses within the grain.

An idealized microstructure with regular, 3×3 cubic grains are considered. The geometry and the discretization of the microstructure is shown in Fig. 16(a). Each grain is assigned a random orientation. The microstructure is subjected to uniaxial tension along the X-direction up to 5% macroscopic strain with a strain rate of 0.05/s. The material and properties are taken to be identical to that presented in Section 6.2 and summarized in Tables 1 and 2. The CPFE discretization consists of 10,647 trilinear hexahedra that corresponds to approximately 76,800 degrees of freedom in the resulting discrete system of equations. Two reduced order models, named ROM1 and ROM2, are considered to approximate the response of the idealized microstructure. ROM1 is generated by assigning a part to each grain in the microstructure ($n = 9$), which leads to a system size of 54. In ROM2, the central grain was further partitioned into nine additional parts (i.e., $n = 17$ with 102 degrees of freedom) as shown in Fig. 16(b)-(c). Among the nine additional parts, part (1) approximates the behavior within the interior of the grain, parts (3), (5), (6) and (8) represent the behavior along the grain boundary and parts (2), (4), (7) and (9) account for the behavior at the triple junctions. The macroscale discretization of the multiscale models consists of a single tri-linear eight-noded hexahedron element.

The homogenized stress-strain curves obtained by the two models and the direct CPFE simulations are shown in Fig. 17. The overall constitutive behaviors computed by the two models are virtually identical, which points to the relative invariance of grain decomposition

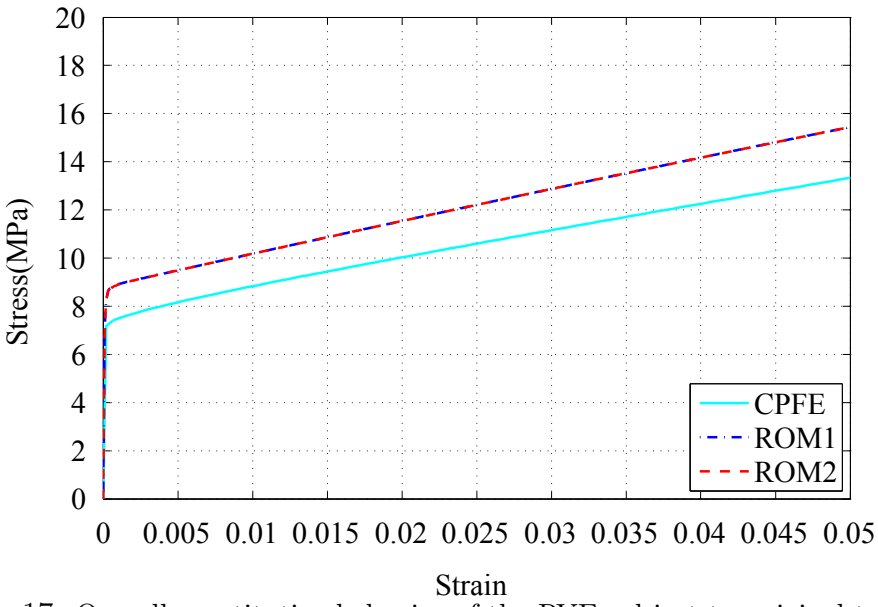

Figure 17: Overall constitutive behavior of the RVE subject to uniaixal tension.

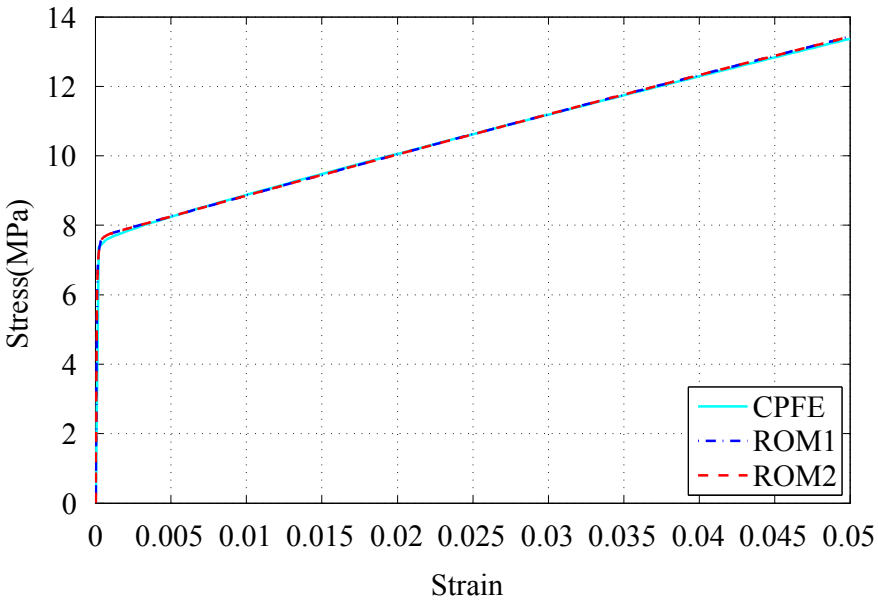

Figure 18: Overall constitutive behavior of the RVE subject to uniaixal tension after parameter scaling.

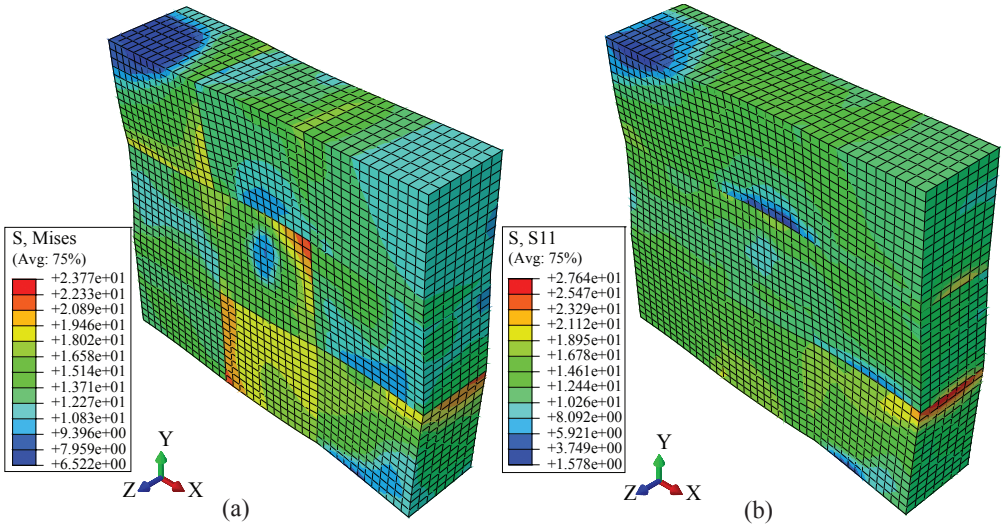

Figure 19: Stress counter of the RVE subject to uniaxial tension along the X direction

on the overall behavior. Both models slightly overestimate the stress-strain behavior as compared to the CPFE simulation, but capture the overall deformation behavior with reasonable accuracy. These results also demonstrate that, in this case, the overall stress-strain behavior is not significantly affected by the order of the reduced order model. Additional analysis of the effect of the model order on accuracy is provided in Ref. [51].

A series of simulations using the same microstructure but with different random set of grain orientations show a consistent trend that reduced order models overestimate the overall stress. In order to differentiate the local stress accuracy from the overall stress accuracy, the initial hardening parameter, $\dot{\gamma}_0$, of the reduced order models is scaled such that the discrepancy between the CPFE and the multiscale models are minimized. The initial hardening parameter was shown to affect the yielding stress and hardening slope as suggested in Ref. [19]. We note that this process also resembles calibration based on experimental data, in which, the reduced order model parameters are set to minimize the discrepancy between the experimental observations and the model predictions. Figure 18 shows the overall stress-strain curves after $\dot{\gamma}_0$ in the reduced order models is set to $30.0s^{-1}$. The overall stress-strain behaviors of the reduced order models and the reference model are virtually identical following the scaling process.

The stress contours within the microstructure as computed by the CPFE model at an applied overall strain magnitude of 5% is shown in Fig. 19. Stresses along the grain boundaries and the triple junctions clearly deviate significantly from the grain interiors, often with significant concentrations at boundaries with high grain orientation mismatch.

Figure 20 compares the evolution of average stress along the X-direction within four subgrains (parts (1), (4), (7) and (9) as shown in Fig. 16) of the central grain in the idealized microstructure. ROM1, does not distinguish between the subgrains of the central grain since the stress is taken to be spatially uniform within the grain. The stress-strain plots for ROM1 is

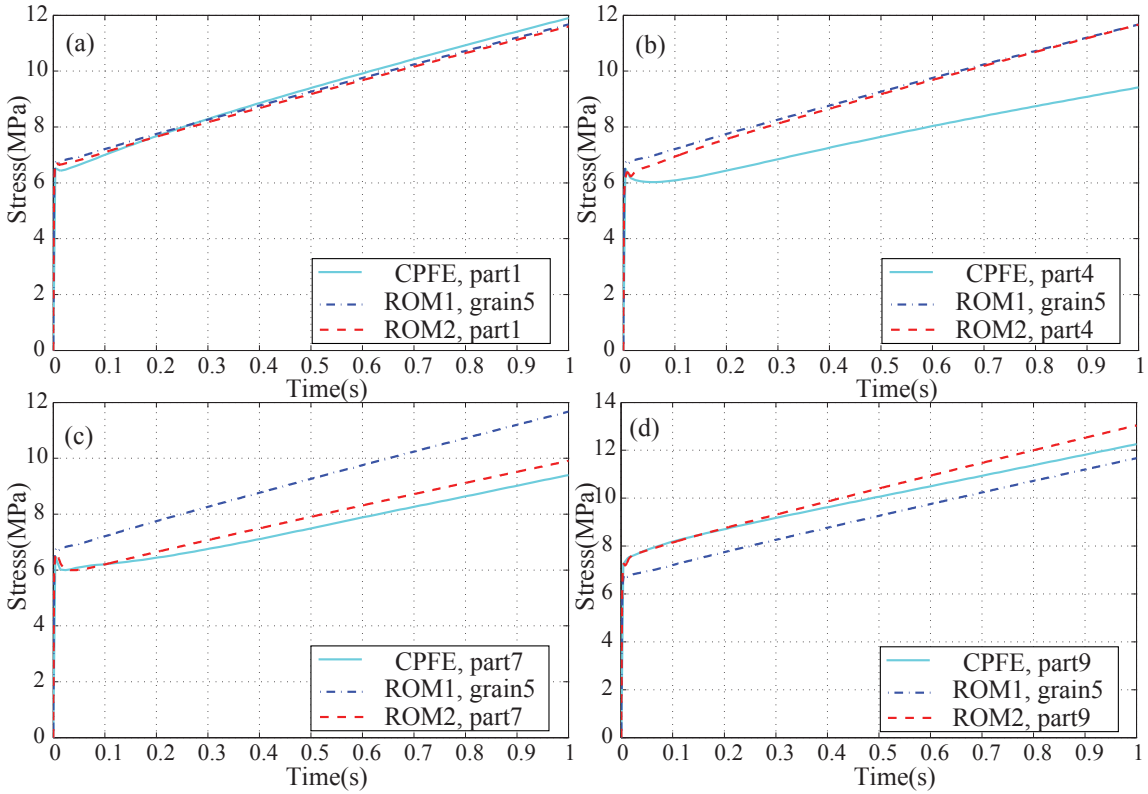

Figure 20: σ_{11} of different parts in grain No. 5.

therefore identical in Figs. 20 (a)-(d). The part average stresses of ROM2 are directly tracked in the evaluation of the model, and therefore readily available. The stresses obtained from CPFE were averaged over the relevant subdomains. Within part (1) of the central grain that corresponds to the grain interior, the stress evolution is very similar to the average stress and the response of both of the proposed models match very well with the CPFE model. The stress within parts (4), (7) and (9) deviate from the average stresses, which are captured reasonably well with ROM2 particularly in parts (7) and (9). While some deviations exist between the CPFE model and the subgrain partitioned ROM2 model, the relative accuracy of the model points to the capability of the proposed approach in capturing stress concentrations within the material microstructure.

6.4 An arch subjected to compression

In this section, a full two-scale analysis is performed to further demonstrate the computational capabilities of the proposed reduced order model. The response of an arch made of aluminum subjected to compressive loading as illustrated in Fig. 22(a) is considered. The geometric model is one half of the arch with inner radius of 30 mm, outer radius of 50 mm and thickness of 5 mm. The top of the arch is cut flat, on which the displacement along the Y direction is applied while the bottom end is fixed. The geometric model is discretized

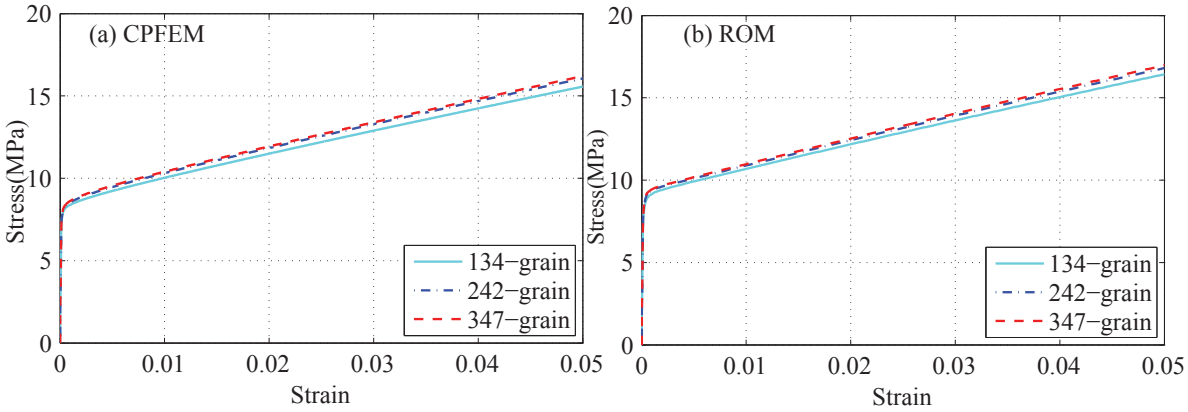

Figure 21: Convergence study on the number of grains in the RVE (a) CPFEM; (b) ROM.

with 56 tri-linear eight-noded hexahedron elements. No comparative analysis based on either direct resolution or computational homogenization could be performed due to prohibitive cost of these approaches.

In order to limit the out-of-plane deformations due to inhomogeneity of the microstructure, a numerical RVE size convergence study is performed. The microstructure characteristics of the arch are taken to be identical to those considered in Section 6.1. Figure 21 shows the stress-strain curves of three different microstructures with 134, 242 and 347 grains, respectively, generated by the proposed approach and CPFE. The stress-strain curves are of single microstructures subjected to uniaxial tension. Figure 21 clearly demonstrates that the two larger microstructures provide near identical responses, which indicates that the 242-grain microstructure is sufficiently representative. The 242-grain microstructure is therefore used in the analysis of the arch.

Figure 22(b) shows the stress contour within the arch at the applied displacement magnitude of 1.425 mm. Under the applied displacement, the structure undergoes significant inelastic deformation as further evidenced by the force-displacement relationship shown in Fig. 23. We note that the inhomogeneity of the stress field is due to the onset of inelastic deformations rather than the microstructure inhomogeneity. No significant out-of-plane deformations are observed in the analysis.

7 Conclusion

We presented a mathematical homogenization scheme for polycrystalline materials which is based on a two-scale asymptotic expansion and the transformation field analysis. The model formulation, computational implementation and numerical verifications were conducted to form a computation framework that can provide overall and local predictions with acceptable accuracy.

Several challenges still remain for the current computational framework. First, a universal

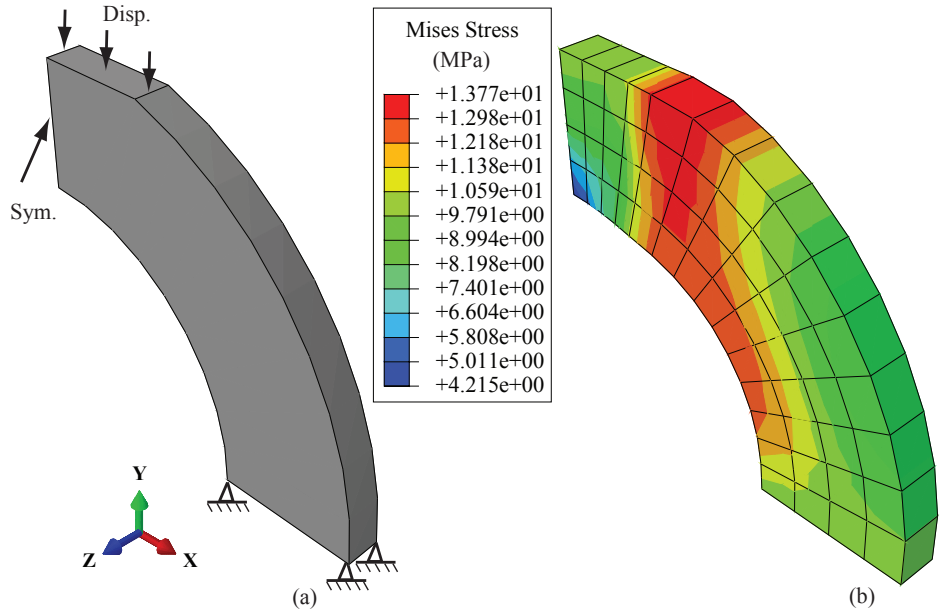

Figure 22: Curve beam: (a) mesh and boundary condtions; (b) von Mises stress contour.

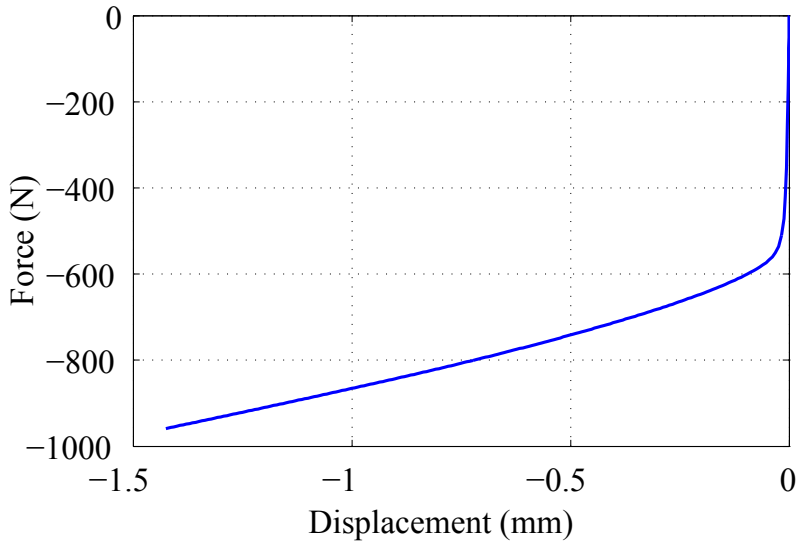

Figure 23: Force-displacement curve of the curved beam example.

grain sub-partitioning technique that can handle a realistic RVE with arbitrary 3D microstructure has not yet been developed. Second, there is no related experimental data used to calibrate the ROM, only a preliminary parameter scaling is investigated instead, which may limit the accuracy of the ROM results. A more complete computational framework including the ROM parameter calibration against experiments is expected to better assess and validate the performance. Third, the current implementation is based on small strain assumption which limits its usage. Expanding to large deformations will gain the capability of mechanical response prediction, as well as texture evolution prediction at finite strain, which will also provide more rigorous validation standard for the accuracy of the reduced order model.

8 Acknowledgement

The authors gratefully acknowledge the research funding from the Air Force Office of Science Research Multi-Scale Structural Mechanics and Prognosis Program (Grant No: FA9550-13-1-0104. Program Manager: Dr. David Stargel). We acknowledge the technical cooperation of the Structural Science Center of the Air Force Research Laboratory, Structural Sciences Center. The authors would also like to acknowledge Dr. Cerrone from Cornell University for sharing his PPM software for microstructure volume mesh generation.

References

[1] J. Aboudi. A continuum theory for fiber-reinforced elastic-viscoplastic composites. *Int. Eng. Sci.*, 20(5):605–621, 1982.

[2] L. Anand. Constitutive equations for the rate-dependent deformation of metals at elevated temperatures. *J. Eng. Mater. Technol.*, 104(1):12–17, 1982.

[3] L. Anand and C. Su. A theory for amorphous viscoplastic materials undergoing finite deformations, with application to metallic glasses. *J. Mech. Phys. Solids*, 53:1362–1396, 2005.

[4] A. Bensoussan, J.-L. Lions, and G. Papanicolaou. *Asymptotic analysis for periodic structures*. North-Holland, Amsterdam, 1978.

[5] T.R. Bieler, P. Eisenlohr, F. Roters, D. Kumar, D.E. Mason, M.A. Crimp, and D. Raabe. The role of heterogeneous deformation on damage nucleation at grain boundaries in single phase metals. *Int. J. Plast.*, 25:1655 – 1683, 2009.

[6] A. Cerrone, J. Tucker, C. Stein, A. Rollett, and A. Ingraffea. Micromechanical modeling of ren88dt:from characterization to simulation. In *2012 Joint Conference of the Engineering Mechanics Institute and the 11th ASCE Joint Specialty Conference on Probabilistic Mechanics and Structural Reliability*, 2012.

[7] R. Courant and D. Hilbert. *Methods of Mathematical Physics*, volume 1. Wily-VCH, 1991.

[8] C.F.O. Dahlberg, J. Faleskog, C.F. Niordson, and B.N. Legarth. A deformation mechanism map for polycrystals modeled using strain gradient plasticity and interfaces that slide and separate. *Int. J. Plast.*, 43(0):177–195, 2013.

[9] F.P.E. Dunne, A.J. Wilkinson, and R. Allen. Experimental and computational studies of low cycle fatigue crack nucleation in a polycrystal. *Int. J. Plast.*, 23(2):273 – 295, 2007.

[10] G.J. Dvorak and Y. Benveniste. On transformation strains and uniform fields in multiphase elastic media. *Proc. R. Soc. Lond. A*, 437:291–10, 1992.

[11] W. E and B. Engquist. The heterognous multiscale methods. *Commun. Math. Sci.*, 1(1): 87–132, 2003.

[12] P. Eisenlohr, M. Diehl, R.A. Lebensohn, and F. Roters. A spectral method solution to crystal elasto-viscoplasticity at finite strains. *Int. J. Plast.*, 46:37–53, 2013.

[13] J. D. Eshelby. The determination of the elastic field of an ellipsoidal inclusion, and related problems. *Proc. R. Soc. Lond. A*, 241(1226):376–396, 1957.

[14] F. Feyel. A multilevel finite element method (FE2) to describe the response of highly non-linear structures using generalized continua. *Comput. Methods Appl. Mech. Engrg.*, 192:3233–3244, 2003.

[15] F. Feyel and J.L. Chaboche. FE2 multiscale approach for modelling the elastoviscoplastic behaviour of long fibre sic/ti composite materials. *Comput. Methods Appl. Mech. Engrg.*, 183:309–330, 2000.

[16] J. Fish, V. Filonova, and Z. Yuan. Reduced order computational continua. *Comput. Methods Appl. Mech. Engrg.*, 221-222:104–116, 2012.

[17] F. Fritzen and M. Leuschner. Reduced basis hybrid computational homogenization based on a mixed incremental formulation. *Comput. Methods Appl. Mech. Engrg.*, 260:143–154, 2013.

[18] M. Groeber and M. Jackson. Dream.3d: A digital representation environment for the analysis of microstructure in 3d. *Integr. Mater. Manuf. Innov.*, 3:5–19, 2014.

[19] S. Groh, E.B. Marin, M.F. Horstemeyer, and H.M. Zbib. Multiscale modeling of the plasticity in an aluminum single crystal. *Int. J. Plast.*, 25:1456–1473, 2009.

[20] J.A. Hernandez, J. Oliver, A.E. Huespe, M.A. Caicedo, and J.C. Cante. High-performance model reduction techniques in computational multiscale homogenization. *Comput. Methods Appl. Mech. Engrg.*, 276:149–189, 2014.

[21] T.Y. Hou and X. Wu. A multiscale finite element method for elliptic problems in composite materials and porous media. *J. Comput. Phys.*, 134:169–189, 1997.

[22] P.V. Houtte. On the equivalence of the relaxed taylor theory and the bishop-hill theory for partially constrained plastic deformation of crystals. *Mater. Sci. Eng. A*, 55(1):69–77, 1982.

[23] P.V. Houtte, S. Li, M. Seefeldt, and L. Delannay. Deformation texture prediction: from the taylor model to the advanced lamel model. *Int. J. Plast.*, 21(3):589–624, 2005.

[24] T. Hui and C. Oskay. A nonlocal homogenization model for wave dispersion in dissipative composite materials. *Int. J. Solids Struct.*, 50(1):38–48, 2013.

[25] T. Hui and C. Oskay. A high order homogenization model for transient dynamics of heterogeneous media including micro-inertia effects. *Comput. Methods Appl. Mech. Engrg.*, 273:181–203, 2014.

[26] T. Hui and C. Oskay. Laplace-domain, high-order homogenization for transient dynamic response of viscoelastic composites. *Int. J. Numerical Methods Eng.*, pages n/a–n/a, 2015.

[27] J.Guedes and N. Kikuchi. Preprocessing and postprocessing for materials based on the homogenization method with adaptive finite element methods. *Comput. Methods Appl. Mech. Engrg.*, 83(2):143–198, 1990.

[28] M. Knezevic and D. J. Savage. A high-performance computational framework for fast crystal plasticity simulations. *Comput. Mater. Sci.*, 83:101–106, 2014.

[29] M. Knezevic, H. F. Al-Harbi, and S. R. Kalidindi. Crystal plasticity simulations using discrete fourier transforms. *Acta Mater.*, 57(6):1777–1784, 2009.

[30] M. Knezevic, R. J. McCabe, R. A. Lebensohn, C. N. Tome, C. Liu, M. L. Lovato, and B. Mihaila. Integration of self-consistent polycrystal plasticity with dislocation density based hardening laws within an implicit finite element framework: Application to low-symmetry metals. *J. Mech. Phys. Solids*, 61(10):2034–2046, 2013.

[31] M. Knezevic, B. Drach, M. Ardeljan, and I.J. Beyerlein. Three dimensional predictions of grain scale plasticity and grain boundaries using crystal plasticity finite element models. *Comput. Methods Appl. Mech. Engrg.*, 277:239–259, 2014.

[32] M. Knezevic, M. Zecevic, I. J. Beyerlein, J. F. Bingert, and R. J. McCabe. Strain rate and temperature effects on the selection of primary and secondary slip and twinning systems in HCP zr. *Acta Mater.*, 88:55 – 73, 2015.

[33] E. Kroner. Berechnung der elastischen konstanten des vielkristalls aus den konstanten des einkristalls. *Z. Phys [in German]*, 151:504–18, 1958.

[34] P. Krysl, S. Lall, and J. E. Marsden. Dimensional model reduction in non-linear finite element dynamics of solids and structures. *Int. J. Numerical Methods Eng.*, 51:479–504, 2001.

[35] R.A. Lebensohn. N-site modeling of a 3d viscoplastic polycrystal using fast fourier transform. *Acta Mater.*, 49:2723–2737, 2001.

[36] R.A. Lebensohn and C.A. Tome. A self-consistent anisotropic approach for the simulation of plastic deformation and texture development of polycrystals: Application to zirconium alloys. *Acta Metall. Mater.*, 41:2611–2624, 1993.

[37] R.A. Lebensohn, A.K. Kanjarla, and P. Eisenlohr. An elasto-viscoplastic formulation based on fast fourier transforms for the prediction of micromechanical fields in polycrystalline materials. *Int. J. Plast.*, 3233:59–69, 2012.

[38] H. Li, C. Wu, and H. Yang. Crystal plasticity modeling of the dynamic recrystallization of two-phase titanium alloys during isothermal processing. *Int. J. Plast.*, 51(0):271–291, 2013.

[39] E.B. Marin and P.R. Dawson. On modelling the elasto-viscoplastic response of metals using polycrystal plasticity. *Comput. Methods Appl. Mech. Engrg.*, 165:1–21, 1998.

[40] K. Mathur and P. Dawson. On modeling the development of crystallographic texture in bulk forming processes. *Int. J. Plast.*, 5(1):67–94, 1989.

[41] F. Meier, C. Schwarz, and E. Werner. Crystal-plasticity based thermo-mechanical modeling of al-components in integrated circuits. *Comput. Mater. Sci.*, 94(0):122–131, 2014.

[42] F.T. Meissonnier, E.P. Busso, and N.P. O'Dowd. Finite element implementation of a generalised non-local rate-dependent crystallographic formulation for finite strains. *Int. J. Plast.*, 17(4):601–640, 2001.

[43] J. C. Michel, H. Moulinec, and P. Suquet. A computational scheme for linear and nonlinear composites with arbitrary phase contrast. *Int. J. Numerical Methods Eng.*, 52(1-2): 139–160, 2001.

[44] J.C. Michel and P. Suquet. Nonuniform transformation field analysis. *Int. J. Solids Struct.*, 40(25):6937–6955, 2003. Special issue in Honor of George J. Dvorak.

[45] J.C. Michel and P. Suquet. Computational analysis of nonlinear composite structures using the nonuniform transformation field analysis. *Comput. Methods Appl. Mech. Engrg.*, 193(48-51):5477–5502, 2004. Advances in Computational Plasticity.

[46] J.C. Michel, H. Moulinec, and P. Suquet. Effective properties of composite materials with periodic microstructure: a computational approach. *Comput. Methods Appl. Mech. Engrg.*, 172:109–143, 1999.

[47] H. Moulinec and P. Suquet. A numerical method for computing the overall response of nonlinear composites with complex microstructure. *Comput. Methods Appl. Mech. Engrg.*, 157:69–94, 1998.

[48] V.D. Nguyen, E. Bechet, C. Geuzaine, and L. Noels. Imposing periodic boundary condition on arbitrary meshes by polynomial interpolation. *Comput. Mater. Sci.*, 55:390–406, 2012.

[49] C. Oskay. Variational multiscale enrichment for modeling coupled mechano-diffusion problems. *Int. J. Numerical Methods Eng.*, 89(6):686–705, 2012.

[50] C. Oskay. Variational multiscale enrichment method with mixed boundary conditions for modeling diffusion and deformation problems. *Comput. Methods Appl. Mech. Engrg.*, 264 (0):178–190, 2013.

[51] C. Oskay and J. Fish. Eigendeformation-based reduced order homogenization for failure analysis of heterogeneous materials. *Comput. Methods Appl. Mech. Engrg.*, 196:1216–1243, 2007.

[52] D. Peirce, R.J. Asaro, and A. Needleman. An analysis of nonuniform and localized deformation in ductile single crystals. *Acta Metall.*, 30:1087–1119, 1982.

[53] D. Peirce, R.J. Asaro, and A. Needleman. Material rate dependence and localized deformation in crystalline solids. *Acta Metall.*, 31:1951–1976, 1983.

[54] R. Quey, P.R. Dawson, and F. Barbe. Large-scale 3d random polycrystals for the finite element method: Generation, meshing and remeshing. *Comput. Methods Appl. Mech. Engrg.*, 200:1729–1745, 2011.

[55] R.Crouch and C. Oskay. Symmetric mesomechanical model for failure analysis of heterogeneous materials. *Int. J Multiscale. Com.*, 8(5):447–461, 2010.

[56] J.R. Rice. Inelastic constitutive relations for solids: An internal-variable theory and its application to metal plasticity. *J. Mech. Phys. Solids*, 19:433–455, 1971.

[57] F. Roters, P. Eisenlohr, L. Hantcherli, D.D. Tjahjanto, T.R. Bieler, and D. Raabe. Overview of constitutive laws, kinematics, homogenization and multiscale methods in crystal plasticity finite-element modeling: Theory, experiments, applications. *Acta Mater.*, 58(4):1152–1211, 2010.

[58] E. Sanchez-Palencia. Lecture notes in physics, vol. 127. Springer-Verlag Berlin, 1980.

[59] J. Segurado, R. A. Lebensohn, J. LLorca, and C. N. Tome. Multiscale modeling of plasticity based on embedding the viscoplastic self-consistent formulation in implicit finite elements. *Int. J. Plast.*, 28(1):124–140, 2012.

[60] A. Staroselsky and L. Anand. Inelastic deformation of polycrystalline face centered cubic materials by slip and twinning. *J. Mech. Phys. Solids*, 46:671–696, 1998.

[61] P. Thamburaja and L. Anand. Polycrystalline shape-memory materials: effect of crystallographic texture. *J. Mech. Phys. Solids*, 49:709–737, 2001.

[62] J. Thomas, M. Groeber, and S. Ghosh. Image-based crystal plasticity fe framework for microstructure dependent properties of ti-6al-4v alloys. *Mater. Sci. Eng. A*, 553:164–175, 2012.

[63] S. Tian, J. Xie, X. Zhou, B. Qian, J. Jun, L. Yu, and W. Wang. Microstructure and creep behavior of FGH95 nickel-base superalloy. *Mater. Sci. Eng. A*, 528:2076–2084, 2011.

[64] S. Turteltaub, S. Yadegari, and A. Suiker. Grain cluster mthod for multiscale simulations of multiphase steels. In *11th World Congress on Computational Mechanicy*, 2014.

[65] Z. Yuan and J. Fish. Multiple scale eigendeformation-based reduced order homogenization. *Comput. Methods Appl. Mech. Engrg.*, 198:2016–2038, 2009.

[66] J. Yvonnet and Q.-C. He. The reduced model multiscale method (r3m) for the non-linear homogenization of hyperelastic media at finite strains. *J. Comput. Phys.*, 223(1):341–368, 2007.

[67] J. Yvonnet, D. Gonzalez, and Q.-C. He. Numerically explicit potentials for the homogenization of nonlinear elastic heterogeneous materials. *Comput. Methods Appl. Mech. Engrg.*, 198:2723–2737, 2009.

[68] M. Zecevic, R. J. McCabe, and M. Knezevic. Spectral database solutions to elasto-viscoplasticity within finite elements: Application to a cobalt-based fcc superalloy. *Int. J. Plast.*, 70:151–165, 2015.

[69] M. Zecevic, R. J. McCabe, and M. Knezevic. A new implementation of the spectral crystal plasticity framework in implicit finite elements. *Mech. Mater.*, 84:114–126, 2015.

[70] S. Zhang and C. Oskay. Variational multiscale enrichment method with mixed boundary conditions for elasto-viscoplastic problems. *Comp. Mech.*, 55(4):771–787, 2015.